Monthly Notices
of the
ROYAL ASTRONOMICAL SOCIETY

Mon. Not. R. Astron. Soc. **421,** 2054–2078 (2012) doi:10.1111/j.1365-2966.2012.20454.x

Magnetoelastic oscillations of neutron stars with dipolar magnetic fields

Michael Gabler,[1,2,3]★ Pablo Cerdá-Durán,[1] Nikolaos Stergioulas,[2] José A. Font[3] and Ewald Müller[1]

[1]*Max-Planck-Institut für Astrophysik, Karl-Schwarzschild-Str. 1, 85741 Garching, Germany*
[2]*Department of Physics, Aristotle University of Thessaloniki, Thessaloniki 54124, Greece*
[3]*Departamento de Astronomía y Astrofísica, Universitat de València, 46100 Burjassot, Valencia, Spain*

Accepted 2011 December 23. Received 2011 December 12; in original form 2011 September 29

ABSTRACT

By means of two-dimensional, general relativistic magnetohydrodynamical simulations we investigate the oscillations of magnetized neutron star models (magnetars) for one particular dipolar magnetic field configuration including the description of an extended solid crust. The aim of this study is to understand the origin of the quasi-periodic oscillations (QPOs) observed in the giant flares of soft gamma-ray repeaters (SGRs). We confirm our previous findings which showed the existence of three different regimes in the evolution depending on the magnetic field strength: (a) a weak magnetic field regime $B < 5 \times 10^{13}$ G, where crustal shear modes dominate the evolution; (b) a regime of intermediate magnetic fields $5 \times 10^{13} < B < 10^{15}$ G, where Alfvén QPOs are mainly confined to the core of the neutron star and the crustal shear modes are damped very efficiently and (c) a strong field regime $B > 10^{15}$ G, where magnetoelastic oscillations reach the surface and approach the behaviour of purely Alfvén QPOs. When the Alfvén QPOs are confined to the core of the neutron star, we find qualitatively similar QPOs as in the absence of a crust. The lower QPOs associated with the closed field lines of the magnetic field configuration are reproduced as in our previous simulations without crust, while the upper QPOs connected to the open field lines are displaced from the polar axis. The position of these upper QPOs strongly depends on the magnetic field strength. Additionally, we observe a family of edge QPOs and one new upper QPO, which was not previously found in the absence of a crust. We extend our semi-analytic model to obtain estimates for the continuum of the Alfvén oscillations. Our results do not leave much room for a crustal-mode interpretation of observed QPOs in SGR giant flares, but can accommodate an interpretation of these observations as originating from Alfvén-like, global, turning point QPOs (which can reach the surface of the star) in models with mean surface magnetic field strengths in the narrow range of $3.8 \times 10^{15} \lesssim B \lesssim 1.1 \times 10^{16}$ G (for a sample of two stiff equation of state and various masses). This range is somewhat larger than estimates for magnetic field strengths in known magnetars. The discrepancy may be resolved in models including a more complicated magnetic field structure or with models taking superfluidity of the neutrons and superconductivity of the protons in the core into account.

Key words: asteroseismology – MHD – stars: kinematics and dynamics – stars: magnetars – stars: neutron – stars: oscillations.

1 INTRODUCTION

The detection of quasi-periodic oscillations (QPOs) in the giant flares of soft gamma-ray repeaters (SGRs) has raised hopes of drawing conclusions about their interior structure, and thus to increase the understanding of the equation of state (EoS) of matter at supranuclear densities. SGRs are a class of magnetars, i.e. very compact objects with very strong magnetic fields (Duncan & Thompson 1992). They show repeated activity in the soft gamma-ray/hard X-ray spectrum, and as of today giant flares with energies between 10^{44} and 10^{46} erg s^{-1} have been detected in three of these objects. In the decaying X-ray tail of two of these events a number of QPOs have been observed (see Israel et al. 2005; Watts & Strohmayer 2007, for recent reviews). The frequencies of the QPOs are roughly 18, 26, 30, 92, 150, 625 and 1840 Hz for the outburst of SGR 1806−20

★E-mail: miga@mpa-garching.mpg.de

and 28, 53, 84 and 155 Hz for SGR 1900+14. Recently, El-Mezeini & Ibrahim (2010) re-analysed the *Rossi X-ray Timing Explorer* (*RXTE*) observations and claimed that they discovered 84, 103 and 648 Hz QPOs in the normal bursts of SGR 1806−20. With a different method Hambaryan, Neuhäuser & Kokkotas (2011) have also found new QPOs in the data of the SGR 1806−20 giant burst at frequencies 16.9, 21.4, 36.4, 59.0 and 116.3 Hz. If confirmed, these are truly fascinating discoveries as the methods employed will allow one to increase the number of extracted QPO frequencies.

The interpretation of the observed QPOs in terms of oscillations of the magnetar itself seems very promising. It may allow for insight into the properties of these objects and constrain the EoS above nuclear matter density. The first step towards such magnetar asteroseismology would be the identification of the modes of the star which have frequencies in the right range and which could be observable during an outburst. For some time after the discovery of the QPOs in SGR 1900−16 in 1998 the main focus was on the torsional shear oscillations of the solid crust because their frequencies in the range between 10s of Hz for nodeless modes and kHz for $n = 1$ modes match the observed frequencies cited above (see Duncan 1998; Piro 2005; Strohmayer & Watts 2005; Samuelsson & Andersson 2007; Sotani, Kokkotas & Stergioulas 2007; Steiner & Watts 2009, and references therein). From energetic considerations it is very likely that these oscillations are excited during a SGR outburst (Duncan 1998; Levin & van Hoven 2011). Moreover, torsional shear oscillations couple preferably to the exterior magnetosphere (Blaes et al. 1989), where the emission in form of a trapped fireball is supposed to occur (Thompson & Duncan 2001). Therefore, there is a natural channel of how these oscillations may influence the X-ray signal emitted during the flare. However, despite some recent improvements of the models (Steiner & Watts 2009), the order of the frequencies of successive shear modes does not allow for a complete interpretation of all observed QPOs.

Since the publications by Levin (2006) and Glampedakis & Andersson (2006) another possibility has been investigated. These authors show that the crust–core coupling due to the extremely strong magnetic field present in magnetars may have significant impact on the shear oscillations of the crust. It was shown in simplified toy models that the shear modes can be damped very efficiently into a magnetohydrodynamic (MHD) continuum of Alfvén oscillations existing in the core of the neutron star. This idea stimulated further interest in the direction of magnetoelastic oscillations by more detailed toy models (Lee 2007, 2008; Levin 2007). In particular, Levin (2007) showed that due to the coupling through the crust long-lived QPOs can be produced at the turning points or edges of the continuum.

Before studying magnetoelastic oscillations in realistic scenarios it is necessary to understand purely Alfvén oscillations of neutron stars in general relativity. Studies using general relativistic MHD (GRMHD) models without taking an extended crust into account revealed two families of long-lived QPOs in the continuum formed by Alfvén oscillations of dipolar magnetic field configurations (Sotani, Kokkotas & Stergioulas 2008b; Cerdá-Durán, Stergioulas & Font 2009; Colaiuda, Beyer & Kokkotas 2009). Cerdá-Durán et al. (2009) derived a semi-analytic model based on standing waves in the short-wavelength approximation, which reproduces the MHD numerical results with very good agreement. The first family of QPOs, termed upper QPOs, is related to the turning point of the continuum at the open field lines close to the polar axis (see Fig. 1). The second family, the lower QPOs, can be found at the turning point in a region of closed field lines near the equator. In this model the upper QPOs have their maximum amplitudes at the surface of the star and are

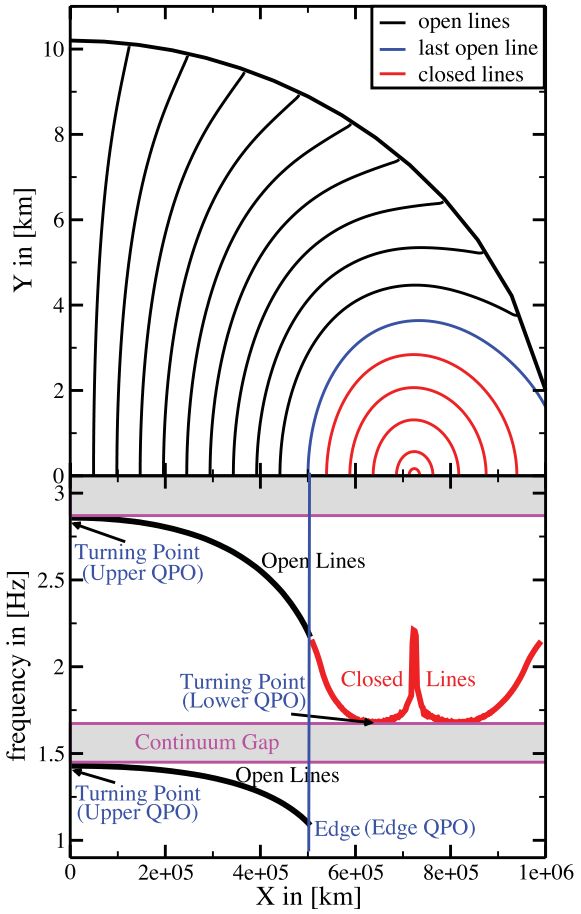

Figure 1. Upper panel: illustration of the dipolar magnetic field configuration including field lines which close inside the neutron star (red lines) and open lines which extend to the exterior (blue and black lines). Lower panel: the frequencies of the corresponding field lines. The ensemble of the frequencies of all field lines forms a continuum with edges and turning points as indicated with the arrows. We call the QPOs related to the turning point of the open field lines upper QPOs, the QPOs related to the turning point of the closed field lines lower QPOs and the QPOs related to the edge of the continuum at the last open field line edge QPOs.

therefore candidates to explain the observed QPOs. The different overtones have frequency ratios given by integer numbers, making them very attractive to explain some of the observed frequencies, such as the 30, 92 and 150 Hz QPOs in SGR 1806−20.

Very recently a few groups have published results considering magnetoelastic oscillations in magnetar models. van Hoven & Levin (2011) have presented a non-relativistic model and shown that the oscillatory spectrum can be influenced significantly by the physical properties of the model. For example the presence of an entangled magnetic field allows for the existence of discrete Alfvén modes, or the decoupling of neutrons in the core from Alfvén waves can change the frequencies of the continuum. In a different approach, based on the coupling between a number of linear one-dimensional wave equations in the core and a two-dimensional wave equation in the crust, Colaiuda & Kokkotas (2011) suggested the existence of global, discrete Alfvén modes in the gaps between continuous parts of the spectrum, as was also suggested in van Hoven & Levin (2011). In that case, the shear modes would not be damped resonantly and they could be observed as QPOs. These oscillations are called gap modes.

In a previous paper (Gabler et al. 2011), we presented a realistic model of magnetoelastic oscillations in magnetars, finding that crustal shear oscillations, often invoked as an explanation of the QPOs seen after giant flares in SGRs, are damped by resonant absorption on time-scales of at most 0.2 s, for a lower limit on the dipole magnetic field strength of 5×10^{13} G. At higher magnetic field strengths (typical in magnetars) the damping time-scale is even shorter. Our findings thus exclude torsional shear oscillations of the crust from explaining the observed low-frequency QPOs. In addition, we found that the Alfvén QPO model is a viable explanation of observed QPOs, if the dipole magnetic field strength exceeds a minimum strength of about 10^{15} G. Then, predominantly Alfvén QPOs are no longer confined to the fluid core, but completely dominate over shear oscillations in the crust region and have a maximum amplitude at the surface of the star.

In the following, we present the details of the extension of a previous model by Cerdá-Durán et al. (2009), where we performed two-dimensional MHD simulations of general relativistic magnetar models with dipolar magnetic fields. As sketched in Gabler et al. (2011) we extend this model by including an extended solid crust, which is able to support shear stresses. Here we complete the corresponding discussion with a larger set of numerical simulations leading to quantitative estimates for the magnetic field strength.

Our results reveal the existence of different regimes depending on the magnetic field strength. For weak magnetic fields $B < 5\times10^{13}$ G we are able to recover purely crustal shear oscillations. At intermediate fields $5 \times 10^{13} < B < 10^{15}$ G crustal modes are damped efficiently and the predominantly Alfvén QPOs are limited to the fluid core of the neutron star. Finally, for strong fields $B > 10^{15}$ G, the magnetoelastic oscillations are no longer confined to the core by the interaction with the solid crust. They reach the surface with significant amplitudes and may be responsible for the observed QPOs. In the analysis presented below we will make substantial use of an extension of the semi-analytic model presented in Cerdá-Durán et al. (2009), which is based on a short-wavelength approximation. We will further study the influence of the EoS on the properties of the equilibrium models, such as the change in frequency of the Alfvén continuum or the dependence of the transition between the different regimes.

The paper is organized as follows. In Section 2 we derive the equations for GRMHD of elastic objects in the 3+1 split of general relativity. Those equations are then simplified to the case of torsional oscillations in the small-amplitude limit. Furthermore, we discuss the boundary conditions we use, and the extension of the semi-analytic model of Cerdá-Durán et al. (2009). Section 3 is concerned with the equilibrium models we use as initial data for our simulations, and in Section 4 we present the numerical methods employed. Section 5 contains the results of our simulation and we discuss our findings in Section 6. Finally, the appendices are devoted to derive an alternative method to compare our results with and to derive the eigenvalue problem of the shear modes in our model.

In equations, we set $c = G = 1$, with c and G being the speed of light and Newton's gravitational constant, respectively. Latin indices run over (r, θ, φ) and Greek indices over (t, r, θ, φ). Partial and covariant derivatives are abbreviated by comma and semicolon, respectively.

2 THEORETICAL FRAMEWORK

In this section we present the equations governing the evolution of torsional shear oscillations of magnetized neutron stars. First, the equations of GRMHD are revised and the effects of an elastic crust up to linear order in the perturbations are included. Next, we apply a number of simplifications for small-amplitude, axisymmetric torsional oscillations. It turns out that these simplifications are equivalent to the so-called anelastic approximation, see Cerdá-Durán et al. (2009). This provides a natural framework that can be used to generalize the formalism in use. The next subsection is concerned with the presentation of the boundary conditions applied in this work, and finally, we sketch the derivation of a semi-analytic model to calculate the Alfvén continuum.

Our numerical approach to study magnetoelastic oscillations of neutron stars is based on an approximate Riemann solver. Additionally, we have obtained a second method for the evolution of the crust coupled to the Riemann solver in the core. In this alternative method we linearize the governing equations and evolve the resulting wave equation numerically. The results are used as a test to which we can compare our evolution with the Riemann solver method. We give the technical details of this approach in Appendix A.

2.1 General relativistic magnetohydrodynamics and elasticity

We adopt the framework of 3+1 split of general relativity. The general metric can thus be described by the following line element:

$$\mathrm{d}s^2 = -\alpha^2 \mathrm{d}t^2 + \gamma_{ij}(\mathrm{d}x^i + \beta^i \mathrm{d}t)(\mathrm{d}x^j + \beta^j \mathrm{d}t), \tag{1}$$

where α and β^i are called lapse function and shift vector, respectively. For spherically symmetric space–times in isotropic coordinates the 3-metric γ_{ij} is conformally flat and can be related to the spatial flat 3-metric $\hat{\gamma}_{ij}$ by the conformal factor Φ:

$$\gamma_{ij} = \Phi^4 \hat{\gamma}_{ij}. \tag{2}$$

The description of matter in general relativity is based on the stress–energy tensor $T^{\mu\nu}$. For a magnetized perfect fluid with elastic properties, $T^{\mu\nu}$ can be written as a sum of different contributions:

$$T^{\mu\nu} = T^{\mu\nu}_{\mathrm{fluid}} + T^{\mu\nu}_{\mathrm{mag}} + T^{\mu\nu}_{\mathrm{elas}}. \tag{3}$$

The different terms can be expressed as follows:

$$T^{\mu\nu}_{\mathrm{fluid}} = \rho h u^\mu u^\nu + P g^{\mu\nu}, \tag{4}$$

where ρ is the rest-mass density, $h = 1 + \epsilon + P/\rho$ the specific enthalpy, ϵ the specific internal energy, P the isotropic fluid pressure, u^μ the 4-velocity of the fluid and $g^{\mu\nu}$ the metric tensor. Moreover, in the ideal MHD approximation, which we adopt here, the magnetic part is given by

$$T^{\mu\nu}_{\mathrm{mag}} = b^2 u^\mu u^\nu + \frac{1}{2} b^2 g^{\mu\nu} - b^\mu b^\nu, \tag{5}$$

with b^μ being the magnetic 4-vector and $b^2 = b_\mu b^\mu$.

The theory of elasticity in general relativity is based on the fundamental work of Carter & Quintana (1972) and was recently extended in a series of papers by Karlovini & Samuelsson (2003, 2004, 2007) and Karlovini, Samuelsson & Zarroug (2004). Our approach follows Carter & Samuelsson (2006). At the linear level in the perturbations the elastic effects of a crust enter in the form of the following contribution to the stress–energy tensor:

$$T^{\mu\nu}_{\mathrm{elas}} = -2\mu_{\mathrm{S}} \Sigma^{\mu\nu}. \tag{6}$$

Here we have introduced the shear modulus μ_{S} and the shear tensor $\Sigma^{\mu\nu}$. The Lie derivative of the latter along the 4-velocity $\mathcal{L}_u \Sigma^{\mu\nu}$ is related to the strain tensor $\sigma^{\mu\nu}$:

$$\mathcal{L}_u \Sigma^{\mu\nu} = \sigma^{\mu\nu}, \tag{7}$$

which is defined as

$$\sigma^{\mu\nu} := \frac{1}{2}\left(u^\mu_{;\alpha} h^{\alpha\nu} + u^\nu_{;\alpha} h^{\alpha\mu}\right) - \frac{1}{3} h^{\mu\nu} u^\alpha_{;\alpha}, \tag{8}$$

where

$$h^{\mu\nu} := g^{\mu\nu} + u^\mu u^\nu \tag{9}$$

is a projection perpendicular to the 4-velocity.

The conservation of energy and momentum $\nabla_\nu T^{\mu\nu} = 0$ and the baryon number conservation $\nabla_\nu J^\nu = 0$ together with Maxwell's equations $\nabla_\nu {}^*F^{\mu\nu} = 0$ and $\nabla_\nu F^{\mu\nu} = 4\pi\mathcal{J}^\mu$ (when expressed in the ideal MHD approximation) lead to the following form of a flux-conservative hyperbolic system of equations:

$$\frac{1}{\sqrt{-g}}\left(\frac{\partial\sqrt{\gamma}U}{\partial t} + \frac{\partial\sqrt{-g}F^i}{\partial x^i}\right) = S. \tag{10}$$

The quantities just introduced are the Faraday electromagnetic tensor field $F^{\mu\nu}$, and its dual ${}^*F^{\mu\nu}$, the rest-mass current $J^\mu := \rho u^\mu$ and the electric 4-current $\mathcal{J}^\mu$, while $\sqrt{-g} = \alpha\sqrt{\gamma}$ and $\gamma = \det(\gamma_{ij})$. The state vector U, the flux vector F^i and the sources S are given by

$$U = [D, S_j, \tau, B^k], \tag{11}$$

$$F^i = \begin{bmatrix} D\hat{v}^i \\ S_j\hat{v}^i + \delta^i_j\left(P + \frac{1}{2}b^2\right) - \frac{b_j B^i}{W} - 2\mu_{\rm S}\Sigma^i_j \\ \tau\hat{v}^i + \hat{v}^i\left(P + \frac{1}{2}b^2\right) - \frac{\alpha b^t B^i}{W} \\ \hat{v}^i B^k - \hat{v}^k B^i \end{bmatrix}, \tag{12}$$

$$S = \left[0, \frac{1}{2}T^{\mu\nu}\frac{\partial g_{\mu\nu}}{\partial x^j}, \alpha T^{\mu\nu}\left(\delta^t_\nu\frac{\partial \ln\alpha}{\partial x^\mu} - \Gamma^t_{\nu\mu}\right), 0, 0, 0\right], \tag{13}$$

where $\hat{v}^i \equiv v^i - \beta^i/\alpha$ and $W = \alpha u^t$ is the Lorentz factor. Additionally, we introduce the 3-velocity of the fluid v^i, the generalized rest-mass density D, the momentum density S_i and the energy density τ:

$$D = \rho W, \tag{14}$$

$$S_i = (\rho h + b^2)W^2 v_i - \alpha b_i b^t, \tag{15}$$

$$\tau = (\rho h + b^2)W^2 - \left(P + \frac{1}{2}b^2\right) - \alpha^2(b^t)^2 - D. \tag{16}$$

The relation between B^i, the magnetic field measured by an Eulerian observer, and the magnetic 4-vector b^μ is given by

$$b^\mu = \left[\frac{W B^i v_i}{\alpha}, \frac{B^i + W^2 v^j B_j \hat{v}^i}{W}\right]. \tag{17}$$

The fluxes defined in equation (12) depend on the shear tensor $\Sigma^{\mu\nu}$ which itself is not a function of the conserved variables U. To complete the system (10) it is thus necessary to describe how the components of the shear tensor evolve with time. For simplicity, we will postpone the discussion of these terms to the next section, where we first apply some simplifications.

2.2 Torsional oscillations in the small-amplitude limit and the anelastic approximation

This work is concerned with torsional oscillations of neutron stars. Therefore we are allowed to perform a number of simplifications to the full set of ideal GRMHD equations presented above.

(i) The temperature of an old neutron star is well below the Fermi temperature, i.e. a barotropic EoS describes the matter with sufficient accuracy. Hence, the equation for the energy density τ in system (10) becomes redundant.

(ii) For purely poloidal background fields and in axisymmetry, the torsional oscillations decouple at the linear level from the polar ones. For small-amplitude oscillations it is thus justified to evolve B^φ and S_φ separately, and to keep B^r, B^θ, S_r and S_θ constant in time.

(iii) When setting the initial velocities in the r and θ directions, and therefore the polar perturbations, to zero, they remain zero during the evolution [see (ii)]. The continuity equation reduces to

$$\frac{\partial\sqrt{\gamma}D}{\partial t} + \frac{\partial D\hat{v}^\varphi}{\partial x^\varphi} = \frac{\partial\sqrt{\gamma}D}{\partial t} = 0, \tag{18}$$

because we assume axisymmetry, i.e. the density D stays constant throughout the evolution.

(iv) Because we are dealing with torsional oscillations, which do not involve large density changes, see (iii), and which only couple very weakly to the space–time evolution, the Cowling approximation should hold, i.e. the metric can be regarded as fixed. Furthermore, the matter distribution and thus the space–time can be regarded as spherically symmetric, since the deviations from sphericity due to the magnetic field are small for the magnetic fields considered here (see Bocquet et al. 1995). In the case of isotropic coordinates and for non-rotating stars this implies that the shift vector vanishes, $\beta^i = 0$, and consequently $\hat{v}^i = v^i$.

In general, the eigenvalues of the flux-vector Jacobians of the system (10) depend on the metric tensor, the conserved variables and the speed of sound. The latter dependence strongly limits the numerical time-step, slowing down any time-explicit numerical simulation. To overcome this limitation in a more general context, Bonazzola, Villain & Bejger (2007) suggested to remove all pressure dependencies from the fluxes F^i, which is known as the anelastic approximation. This changes the properties of the eigenvalues of the system making them independent of the speed of sound. In our case, as a consequence of (iii), the eigenvalues of the flux-vector Jacobians of the system (10) do no longer depend on the speed of sound (see below in this section) and the numerical time-step is thus set by the speed of Alfvén waves only.

The anelastic approximation provides a natural generalization of the method applied in the present work. It allows one to describe situations also involving perturbations in density and pressure, and to study more complicated magnetic field configurations including the coupling between axial and polar oscillations, as a first step towards full three-dimensional simulations. This is, however, beyond the scope of the present work.

To summarize, we only evolve the equations for S_φ and B^φ and hold all other conserved variables of equation (11) constant. Together with equation (10) the following definitions describe the evolution of torsional oscillations of magnetized neutron stars including an elastic crust:

$$U = [S_\varphi, B^\varphi], \tag{19}$$

$$F^r = \left[-\frac{b_\varphi B^r}{W} - 2\mu_{\rm S}\Sigma^r_\varphi, -v^\varphi B^r\right], \tag{20}$$

$$F^\theta = \left[-\frac{b_\varphi B^\theta}{W} - 2\mu_{\rm S}\Sigma^\theta_\varphi, -v^\varphi B^\theta\right], \tag{21}$$

$$S = [0, 0]. \tag{22}$$

To derive the shear tensor $\Sigma^{\mu\nu}$ for torsional oscillations in the small-amplitude limit, we follow Schumaker & Thorne (1983). Since we assume the Cowling approximation to hold, a diagonal metric $g^{\mu\nu} = \mathrm{diag}(g^{\mu\nu})$, and restrict our considerations to linear

order in the displacements, the components of $\Sigma^{\mu\nu}$ can be written as

$$\Sigma^{ij} = \frac{1}{2\alpha}[g^{ik}(\xi^j\alpha)_{,k} + g^{jk}(\xi^i\alpha)_{,k}] - \frac{g^{ij}}{3\alpha}(\xi^k\alpha)_{,k}, \tag{23}$$

while the other components vanish, $\Sigma^{\mu t} = \Sigma^{tv} = 0$. Here, the displacement ξ^j has been introduced. The corresponding time derivative is related to the 3-velocity of the fluid as follows:

$$\xi^j_{,t} = \alpha v^j = \frac{u^j}{u^t}. \tag{24}$$

For purely torsional oscillations the more general expression in equation (23) simplifies to

$$\Sigma^{ij} = \frac{1}{2}\begin{bmatrix} 0 & 0 & g^{rr}\xi^\varphi_{,r} \\ 0 & 0 & g^{\theta\theta}\xi^\varphi_{,\theta} \\ g^{rr}\xi^\varphi_{,r} & g^{\theta\theta}\xi^\varphi_{,\theta} & 0 \end{bmatrix}. \tag{25}$$

In its current form the system of equations (10) and (19)–(22) is incomplete, because the displacement appears in the fluxes, equations (20) and (21). Hence, it is necessary to add (at least) one equation for the evolution of ξ^φ. During the calculations it turned out that the direct integration of ξ^φ via equation (24) is numerically disadvantageous because of several reasons.

(i) The use of ξ^φ requires an evaluation of its spatial derivatives when calculating the fluxes in equations (19)–(22). This leads to numerical inaccuracies in regions where the displacement changes strongly.

(ii) Alternatively one could move the additional terms including the derivatives of ξ^φ to the source terms of the system of equations. However, it is numerically more desirable to have a system of conservation laws without any source terms. Furthermore, the spatial derivatives of the shear modulus μ_S would appear in the source terms, which might give rise to spurious oscillations, because μ_S is given in tabulated form.

(iii) The interface conditions at the crust–core interface are given in terms of ξ^φ and $\xi^\varphi_{,r}$. It turns out that it is numerically difficult to impose them directly on ξ^φ ensuring a sufficiently accurate corresponding condition for its radial derivative (see end of Section 4).

Therefore, instead of evolving ξ^φ, the system of equation (10) with equations (19)–(22) is supplemented with the following equations for the spatial derivatives of ξ^φ:

$$\left(\xi^\varphi_{,r}\right)_{,t} - (v^\varphi\alpha)_{,r} = 0, \tag{26}$$

$$\left(\xi^\varphi_{,\theta}\right)_{,t} - (v^\varphi\alpha)_{,\theta} = 0, \tag{27}$$

which are based on equation (24).

To obtain the eigenvalues we write the complete system in the form of a conservation law like equation (10). This introduces the new conserved variables U, fluxes F^k and sources S:

$$U = \left[S_\varphi, B^\varphi, \left(\alpha\xi^\varphi_{,r}\right), \left(\alpha\xi^\varphi_{,\theta}\right)\right], \tag{28}$$

$$F^k = \begin{bmatrix} -\frac{b_\varphi B^k}{W} - 2\mu_S\Sigma^k_\varphi \\ -v^\varphi B^k \\ -\alpha v^\varphi\delta^k_r \\ -\alpha v^\varphi\delta^k_\theta \end{bmatrix}, \tag{29}$$

$$S = \left[0, 0, -\delta^k_r\frac{\alpha v^\varphi}{\sqrt{-g}}\frac{\partial\sqrt{-g}}{\partial x^k}, -\delta^k_\theta\frac{\alpha v^\varphi}{\sqrt{-g}}\frac{\partial\sqrt{-g}}{\partial x^k}\right], \tag{30}$$

where $k = \{r, \theta\}$. The solution of the eigenvalue problem of the associated flux-vector Jacobian leads to the following non-zero eigenvalues:

$$\lambda^k_{1/2} = \pm\sqrt{\frac{(B^k)^2 + \mu_S/g_{kk}}{A}}, \tag{31}$$

$$A = \frac{\partial S_\varphi}{\partial v_\varphi} = \rho h W^4(1 + v_\varphi v^\varphi) + B^r B_r + B^\theta B_\theta. \tag{32}$$

The set of equations (10) with (28)–(30) is useful for computing the eigenvalues, but contains non-zero sources in the conservation law. For the numerical time evolutions, we thus implement the original set equation (10) with equations (19)–(22) and equations (26) and (27) (see Section 4 for details).

2.3 Boundary conditions at the surface and treatment of the crust–core interface

The system of equations for magnetoelastic torsional oscillations contains two degrees of freedom related to the two non-vanishing eigenvalues (31). Therefore, we have to impose boundary conditions at the surface of the star that mimic the incoming waves from the magnetosphere, which are not included in our simulations. In the core, where $\mu_S = 0$, there are still two degrees of freedom. Since we are simulating both regions (crust and core) having the same number of degrees of freedom there is no need for boundary conditions at the crust–core interface (although there is a need for a special treatment for numerical reasons, see below).

In addition, in the case of ideal MHD without charges, the electric field is continuous everywhere, and hence the velocity v^φ, too. This implies continuity of the displacement, ξ^φ, and of its time derivative, $\xi^\varphi_{,t}$. At the surface of the star and at the crust–core interface the tangential derivative, $\xi^\varphi_{,\theta}$, is continuous, while no restrictions apply to the continuity of $\xi^\varphi_{,r}$.

Boundary conditions at the surface. We assume that there are no current sheets at the surface of the star, i.e. the tangential magnetic field components have to be continuous,

$$b^\varphi_{\rm crust} = b^\varphi_{\rm atmosphere}, \tag{33}$$

at the surface.

The conservation of momentum gives the continuity of the traction t^φ:

$$t^\varphi = T(\tilde{\boldsymbol{n}}, \tilde{\boldsymbol{\varphi}}) = T(\tilde{\boldsymbol{r}}, \tilde{\boldsymbol{\varphi}}) = T^{r\varphi}, \tag{34}$$

i.e. the tangential stresses inside and outside the star have to balance each other. Here the tilde indicates normalized vectors, $\tilde{\boldsymbol{n}}$ is the normal to the surface of the star and thus $\tilde{\boldsymbol{n}} = \tilde{\boldsymbol{r}}$.

The continuous traction condition can be simplified in the case of continuous b^φ and leads to a condition for $\xi^\varphi_{,r}$:

$$T^{r\varphi}_{\rm crust} = T^{r\varphi}_{\rm atmosphere}, \tag{35}$$

$$b^r b^\varphi_{\rm crust} + \frac{\mu_S}{\Phi^4}\xi^\varphi_{{\rm crust},r} = b^r b^\varphi_{\rm atmosphere}, \tag{36}$$

$$\xi^\varphi_{{\rm crust},r} = 0. \tag{37}$$

Equations (33) and (37) are the set of boundary conditions that we apply at the surface of the star. We need the additional condition (37), because we are evolving more variables than the degrees of freedom of the system.

The assumptions made here are motivated by the picture that the magnetospheric field close to the surface will move with its

footpoints in the crust, i.e. the exterior solution relaxes to a force-free field on a much shorter time-scale than the interior evolves. This implies that currents can be maintained in the magnetosphere, which is necessary to support more general equilibrium configurations than considered here and hence to create a twisted magnetospheric field. A more detailed discussion of the coupling to the magnetosphere would exceed the scope of this paper and will be purpose of further investigations.

Our boundary conditions are similar to those used in previous work without the presence of a crust (Sotani et al. 2008b; Cerdá-Durán et al. 2009; Colaiuda et al. 2009) and in simulations with a crust (Colaiuda & Kokkotas 2011; Gabler et al. 2011). However, our boundary conditions differ from those of Lander, Jones & Passamonti (2010) and Lander & Jones (2011) who choose a particular set of variables vanishing at the surface of the neutron star, which defines the corresponding boundary conditions. Other approaches (Braithwaite & Nordlund 2006; Ciolfi et al. 2011; Lasky et al. 2011) involve the evolution of some parts of the neutron star's atmosphere. For purely toroidal oscillations it is possible, however, to impose appropriate boundary conditions and to avoid that evolution.

The *treatment of the crust–core interface* requires particular attention. At this interface no boundary conditions are required and by knowing the variables at one instant of time on both sides (crust and core) one should be able to evolve the system. However, the stability of the employed schemes turned out to depend sensitively on the particular treatment of the reconstruction of the variables, which are allowed to be discontinuous or to have discontinuous spatial derivatives (see below). In the following we will describe how to proceed to achieve stable evolutions.

As anywhere else the traction is supposed to be continuous:

$$T^{r\varphi}_{\rm core} = T^{r\varphi}_{\rm crust}, \tag{38}$$

$$-b^r b^\varphi_{\rm core} = -b^r b^\varphi_{\rm crust} - \frac{\mu_{\rm S}}{\Phi^4}\xi^\varphi_{,r}. \tag{39}$$

This can be transformed by virtue of the linearized induction equation

$$b^\varphi = b^r \xi^\varphi_{,r} + b^\theta \xi^\varphi_{,\theta}\,, \tag{40}$$

the continuity of the displacement, and thus $\xi^\varphi_{{\rm core},\theta} = \xi^\varphi_{{\rm crust},\theta}$, into

$$\begin{aligned} &b^r\left(b^r\xi^\varphi_{{\rm core},r} + b^\theta\xi^\varphi_{{\rm core},\theta}\right) \\ &\quad = b^r\left(b^r\xi^\varphi_{{\rm crust},r} + b^\theta\xi^\varphi_{{\rm crust},\theta}\right) + \tfrac{\mu_{\rm S}}{\Phi^4}\xi^\varphi_{{\rm crust},r}, \end{aligned} \tag{41}$$

$$\xi^\varphi_{{\rm core},r} = \left(1 + \frac{\mu_{\rm S}}{\Phi^4 (b^r)^2}\right)\xi^\varphi_{{\rm crust},r}. \tag{42}$$

In Section 4 we will show how to ensure the continuity of the traction and maintain the correct relation between the radial derivatives of the displacement in the core and in the crust.

Obviously the discontinuous radial derivative allows b^φ to be discontinuous (equation 40). Hence, in general, there are current sheets present at the crust–core interface, which are unavoidable, and a consequence of the coupled evolution and the assumption of ideal MHD.

2.4 Semi-analytic model

A very useful tool to obtain the frequencies of purely magnetic oscillations inside a neutron star was presented by Cerdá-Durán et al. (2009). These authors showed that in the linear regime and in the limit of short wavelengths it is possible to calculate the Alfvén continuum with a semi-analytic model. Here, we will only sketch the method, and for more information we refer to Cerdá-Durán et al. (2009). In the aforementioned limit an Alfvén wave will travel along magnetic field lines corresponding to

$$\frac{{\rm d}\boldsymbol{x}}{{\rm d}t} = \boldsymbol{v}_{\rm a}(\boldsymbol{x}), \tag{43}$$

where $\boldsymbol{v}_{\rm a}$ is the Alfvén velocity. Any displacement Y travelling along the magnetic field lines can be expressed as a function of *magnetic-field-line-adapted* coordinates (χ, ζ) and time, where χ labels the magnetic field line by the radius at which it crosses the equatorial plane, and $\zeta = t(r, \theta; \chi)/t_{\rm tot}(\chi) - 1/2$ is a dimensionless parameter along each field line. Here $t_{\rm tot}(\chi)$ is twice the total travel time of an Alfvén wave travelling along a magnetic field line starting from the equatorial plane and ending at the surface or at another point in the equatorial plane. Note that ζ used in this work corresponds to ξ in Cerdá-Durán et al. (2009), because here ξ denotes the displacement related to the 4-velocity of the fluid. For a travelling wave Y satisfies trivially the wave equation

$$\frac{\partial^2 Y(\chi,\zeta,t)}{\partial t^2} = \frac{1}{t_{\rm tot}(\chi)^2}\frac{\partial^2 Y(\chi,\zeta,t)}{\partial \zeta^2}. \tag{44}$$

Next we assume standing waves of the form

$$Y(\chi,\zeta,t) = a(\chi)\sin(\kappa\zeta + \phi_\zeta)\cos(2\pi f t + \phi_{\rm t}), \tag{45}$$

where κ is the wavenumber, $a(\chi)$ the amplitude, $\phi_{\rm t}$ the temporal phase, ϕ_ζ a spatial phase and f is the oscillation frequency. The dispersion relation then is simply given by

$$f = \frac{\kappa}{2\pi t_{\rm tot}}. \tag{46}$$

At this point the frequencies of the oscillations are completely determined by the magnetic field topology and the boundary conditions.

Cerdá-Durán et al. (2009) did not consider an extended crust, and hence the boundary condition was set at the surface and corresponded to the continuous traction condition. This resulted in a vanishing radial derivative of the displacement and a maximum amplitude of the perturbation at the surface. However, when an extended crust is present there exist two different regimes. For low magnetic field strengths ($B \lesssim 10^{15}$ G) the standing waves show a node at the crust–core interface (Gabler et al. 2011), which may be interpreted as a reflection of the standing wave at the crust–core interface. As we shown below, this change of the boundary condition for the semi-analytic model is necessary to calculate the correct frequencies and to find the symmetry of the numerically obtained QPOs.

For stronger magnetic fields ($B > 10^{15}$ G), the oscillations reach the surface, and we can apply the boundary condition of Cerdá-Durán et al. (2009). In order to take the crust into account the velocity of the perturbation can be approximated by the eigenvalues (31), assuming that the perturbation Y is still travelling along the magnetic field lines. In an intermediate regime at around 10^{15} G we do not expect the semi-analytic model to be valid, because in this case the shear and magnetic contributions to the evolution in the crust are of similar order.

3 EQUILIBRIUM MODELS

The initial models are self-consistent general relativistic equilibrium models of magnetized non-rotating neutron stars with a purely poloidal magnetic field (Bocquet et al. 1995). We use the numerical code 'MAGSTAR' of the LORENE library[1] to compute these models,

[1] http://www.lorene.obspm.fr

which include the effects of the magnetic field on the matter and the space–time.

In our models the magnetic field is generated by a current of the form $\mathcal{J}^{\varphi} = \rho h C$, where C is a constant which determines the strength of the magnetic field. We note that different choices of the current can lead to different internal magnetic fields, still resembling an exterior dipole field (see e.g. van Hoven & Levin 2011). Hereafter, we will label the different models by the surface value of their magnetic field strength at the pole.

As we assume a spherically symmetric space–time and matter background in our simulations we angle average the density of the background model to obtain a spherically symmetric model from the LORENE data. In the most extreme cases, i.e. for a very strong magnetic field this simplification changes the structure of the neutron star by at most about 1 per cent. For example the density at different angles but constant radius varies within less than one per cent at $B = 5 \times 10^{15}$ G. Therefore, the influence on the oscillations is in general less than that of other approximations we are applying.

For the EoS we can choose between different realistic barotropic models including the description of a crust. We use four combinations of two EoS in the core matched to two distinct EoS for the crust. For the core we chose the APR EoS (Akmal, Pandharipande & Ravenhall 1998) and the stiffer EoS L (Pandharipande & Smith 1975), while for the low-density region of the crust we select EoS NV (Negele & Vautherin 1973) and EoS DH (Douchin & Haensel 2001). The recent discovery of a $2\,\mathrm{M}_{\odot}$ neutron star by Demorest et al. (2010) excludes EoS which cannot reproduce such large masses. The properties of the equilibrium models used in this work are summarized in Table 1. These models are a subset of the models used in Sotani et al. (2007). Here, r_{s} and r_{cc} are the radii of the surface of the star and of the crust–core interface, respectively, and $\Delta r_{\mathrm{crust}} = r_{\mathrm{s}} - r_{\mathrm{cc}}$ is the size of the crust. We note that table 1 of Sotani et al. (2007) shows $\Delta r_{\mathrm{crust}}/r_{\mathrm{cc}}$, instead of $\Delta r_{\mathrm{crust}}/r_{\mathrm{s}}$, and thus the percentage for the relative size of the crust is different in their case. However, we checked that the value of $\Delta r_{\mathrm{crust}}$ is the same in both cases. The frequencies of the crustal modes with $n > 0$ depend sensitively on the size of the crust (Samuelsson & Andersson 2007). Therefore, a proper definition of the size of the crust is important.

Table 1. EoS, masses, radii of the star, radii of the crust–core interface and sizes of the crust of the models studied in this paper (without magnetic field).

EoS	Mass ($\mathrm{M}_{\odot}$)	Circumferential radius r_{s} (km)	Inner radius of crust (km)	Relative size of crust $\frac{\Delta r_{\mathrm{crust}}}{r_{\mathrm{s}}}$ (per cent)
APR+DH	1.4	12.10	11.22	7.2
	1.6	12.07	11.38	5.7
	1.8	12.00	11.43	4.8
	2.0	11.90	11.44	3.9
	2.2	11.63	11.31	2.8
APR+NV	1.4	11.94	10.85	9.1
	1.6	11.93	11.07	7.2
	1.8	11.92	11.19	6.1
	2.0	11.81	11.23	4.9
	2.2	11.56	11.12	3.8
L+DH	1.4	14.74	13.33	9.6
	1.6	14.85	13.72	7.6
	1.8	14.93	13.94	6.6
	2.0	14.99	14.13	5.7
	2.2	14.94	14.22	4.8
L+NV	1.4	13.29	11.88	10.6
	1.6	13.58	12.35	9.1
	1.8	13.86	12.76	7.8
	2.0	14.02	13.08	6.7
	2.2	14.12	13.30	5.8

The shear oscillations of the crust are mainly determined by the shear modulus μ_{S} which we obtain from the zero-temperature limit of Strohmayer et al. (1991) given by

$$\mu_{\mathrm{S}} = 0.1194 \frac{n_{\mathrm{i}}(\mathrm{Ze})^2}{a}, \tag{47}$$

where n_{i} is the ion density, (Ze) the ion charge and $a = [3/(4\pi n_{\mathrm{i}})]^{1/3}$ the average ion spacing. This equation is derived for a perfect body-centred cubic (bcc) lattice, and the shear modulus, which has different magnitude along different crystal axes, is averaged in order to obtain an isotropic effective shear modulus μ_{S} (see Strohmayer et al. 1991). For the NV EoS of the crust we use a simple fitting formula derived by Duncan (1998):

$$\mu_{\mathrm{S}} = 1.267 \times 10^{30}\,\mathrm{erg\,cm^{-3}}\,\rho_{14}^{4/5}, \tag{48}$$

where $\rho_{14} = \rho/(10^{14}\,\mathrm{g\,cm^{-3}})$.

To calculate the shear modulus for the DH EoS, one has to evaluate n_{i} in equation (47) in terms of the nucleon number A, the proton number Z and the neutron fraction X_{n} (Piro 2005): $n_{\mathrm{i}} = \rho_{\mathrm{i}} m_{\mathrm{i}}$ and $A\rho_{\mathrm{i}} \sim \rho(1 - X_{\mathrm{n}})$. The composition at a given density is given in Douchin & Haensel (2001). The shear modulus can be estimated to be

$$\mu_{\mathrm{S}} = 1.2 \times 10^{30}\,\mathrm{erg\,cm^{-3}}\,\rho_{14}^{4/3} \left(\frac{Z}{38}\right)^2 \left(\frac{302}{A}\right) \times \left(\frac{1 - X_{\mathrm{n}}}{0.25}\right)^{4/3}. \tag{49}$$

Sotani et al. (2007) introduced the following fit to this equation:

$$\mu_{\mathrm{S}} = 10^{30}\,\mathrm{erg\,cm^{-3}} \left(0.02123 + 0.37631\rho_{14} + 3.13044\rho_{14}^2 - 4.718141\rho_{14}^3 + 2.46792\rho_{14}^4\right). \tag{50}$$

This function provides a good approximation for densities larger than $\rho = 5 \times 10^{11}\,\mathrm{g\,cm^{-3}}$, but below we will rely on the more general expression in equation (49). The main motivation to use this fit is to allow for a direct comparison of the results obtained in this work to the results presented in Sotani et al. (2007) and Colaiuda & Kokkotas (2011).

The crust–core boundary for the NV and DH EoS is defined at $\rho_{\mathrm{cc,NV}} = 2.4 \times 10^{14}\,\mathrm{g\,cm^{-3}}$ and $\rho_{\mathrm{cc,DH}} = 1.28 \times 10^{14}\,\mathrm{g\,cm^{-3}}$, respectively.

We employed two EoS which give neutron star models with large shear moduli compared to other available EoS (Steiner & Watts 2009). Therefore, the results obtained in this work can be regarded as an upper limit for the influence of the crust.

4 NUMERICAL METHODS

This section is devoted to the numerical methods employed to analyse the torsional shear oscillations. The current work is an extension of the study of Cerdá-Durán et al. (2009), whose non-linear GRMHD code we use as a basis for our simulations. The code has been developed in order to investigate various astrophysical scenarios where both magnetic fields and strong gravitational fields play an important role in the evolution of the system. (Dimmelmeier, Font & Müller 2002a,b; Dimmelmeier et al. 2005; Cerdá-Durán et al. 2008). The code uses high-resolution shock-capturing schemes to solve the GRMHD equations for a dynamical space–time, under the approximation of the conformally flat condition (CFC) for the Einstein's equations (Wilson, Mathews & Marronetti 1996; Isenberg

2008). For a spherically symmetric space–time the CFC metric is an exact solution of Einstein's equations, and reduces to the solution in isotropic coordinates. Therefore, this numerical code is well suited to describe the space–time used in the simulations of the present work. The equations are cast in a first-order, flux-conservative hyperbolic form, supplemented by the flux constraint transport method to ensure the solenoidal condition of the magnetic field.

The basic version of the code including the solution of the ideal GRMHD equations was thoroughly tested in Cerdá-Durán et al. (2008), who demonstrate the robustness of the code for a number of stringent tests, such as relativistic shocks, highly magnetized fluids, equilibrium configurations of magnetized neutron stars and the magnetorotational core collapse of a realistic progenitor. One important feature is the ability of the code to handle different classes of EoS which range from simple analytical expressions to microphysically derived tables. We want to emphasize that although the current project is concerned with small-amplitude perturbations in order to apply simplifications appropriate to a linear regime, the code can in principle handle large amplitudes and in general is non-linear.

While the numerical method employed in the original version of the code to integrate the equations is unchanged, we modify the equations to be solved according to equations (10) and (19)–(22) in the crust. As mentioned above we also have to solve for the spatial derivatives of ξ^{φ}. For these equations, which do not represent conservation laws, we calculate the fluxes $-\alpha v^{\varphi}$ corresponding to equations (26) and (27) at the cell interfaces with the corresponding approximate Riemann solver. The derivatives of the fluxes are approximated by dividing the difference of the flux at the two cell interfaces by the grid extension. Although this approach should be able to cope with discontinuities, as present at the crust–core interface for the shear modulus, it turns out that special care has to be taken to achieve a converging method. The coupling between the crust and the core will be described in detail below. We note that when using this approach and setting the shear modulus in the crust to zero the results of Cerdá-Durán et al. (2009) are recovered.

Setting up the interface conditions turned out to be a very delicate issue. The shear modulus is discontinuous at the crust–core interface, and Riemann solvers are able to cope with discontinuities at cell interfaces. Therefore, we define the crust–core interface to be located at a cell interface. In this case it is crucial to ensure that the reconstruction procedure gives a value for $\xi^{\varphi}_{,r} \sim \Sigma^{r}_{\varphi}$ which is consistent with the continuous traction conditions (Section 2.3). Any standard reconstruction method not taking this condition explicitly into account failed and the simulations produced spikes in the radial profiles that spoiled the evolution or even made the whole evolution unstable. The main cause for this behaviour is the discontinuity of the shear modulus at the crust–core interface. For intermediate and weak magnetic fields, the very large shear modulus on one side and the vanishing shear modulus on the other causes the different terms in the momentum equation for the radial flux equation (20) to be much larger on the side of the crust than on the side of the core, i.e.

$$\left|\frac{b_{\varphi}B^{r}}{W}\right|_{\rm crust}, \ \left|\mu_{\rm S}\Sigma^{r}_{\ \varphi}\right|_{\rm crust} \gg \left|-\frac{b_{\varphi}B^{r}}{W}\right|_{\rm core}. \tag{51}$$

The evaluation of the flux at the crust–core interface is numerically problematic due to non-cancellations of the two terms on the side of the crust. However, when taking the continuous traction condition appropriately into account, this problem does not arise and the flux at the core–crust interface is well behaved, allowing one to perform simulations also for intermediate and weak magnetic fields.

We are using the following numerical treatment based on the continuous traction condition $\xi^{\varphi}_{\rm core} = \xi^{\varphi}_{\rm crust} \equiv \xi^{\varphi}$ and $\xi^{\varphi}_{{\rm core},r} = \eta\xi^{\varphi}_{{\rm crust},r}$ with $\eta = 1 + \mu_{\rm S}/(\Phi^4(b^r)^2)$. The derivatives at the crust–core interface can be approximated by

$$\xi^{\varphi}_{{\rm core},r}(r_{\rm cc}) = \frac{\xi^{\varphi}(r_{\rm cc}) - \xi^{\varphi}_{\rm core}(r_{\rm cc} - 0.5\Delta r)}{0.5\Delta r}, \tag{52}$$

$$\xi^{\varphi}_{{\rm crust},r}(r_{\rm cc}) = \frac{\xi^{\varphi}_{\rm crust}(r_{\rm cc} + 0.5\Delta r) - \xi^{\varphi}(r_{\rm cc})}{0.5\Delta r}, \tag{53}$$

where Δr the grid spacing in radial direction. Both equations lead to the following expression for ξ^{φ}:

$$\xi^{\varphi}(r_{\rm cc}) = \frac{\xi^{\varphi}_{\rm core}(r_{\rm cc} - 0.5\Delta r) + \eta\xi^{\varphi}_{\rm crust}(r_{\rm cc} + 0.5\Delta r)}{1+\eta}. \tag{54}$$

Knowing ξ^{φ} at the crust–core interface one can calculate the radial derivatives $\xi^{\varphi}_{{\rm crust},r}$ and $\xi^{\varphi}_{{\rm core},r}$, and finally the fluxes. For the calculations presented in this paper we used a second-order approximation of the derivatives instead of equations (52) and (53).

5 RESULTS

First, we show that our code reproduces the purely shear oscillations of the crust, and we demonstrate how these crustal modes are damped when the magnetic field is switched on. The next two subsections are concerned with the behaviour of the magnetoelastic oscillations at intermediate fields ($5 \times 10^{13} < B < 10^{15}$ G) and at higher magnetic field strengths, respectively. In the remaining subsections we address the issue of different equilibrium models and investigate the magnetic field threshold at which the magnetoelastic QPOs break out of the core and reach the surface of the neutron star. For intermediate magnetic field strengths the QPOs are confined to the core due to the interaction with the crust. If not stated otherwise we refer to the results using an equilibrium model obtained with the APR+DH EoS with a mass of $M = 1.4\,{\rm M}_{\odot}$ (see Table 1).

The two-dimensional simulations are computationally very demanding. On a single Intel Xeon processor with 3 GHz a typical simulation necessary to perform a Fourier analysis of the Alfvén spectrum takes of the order of a few weeks for one equilibrium model. We are therefore restricted in the maximum time we can evolve the models. In the most demanding situation the minimum evolution time corresponds to 10 times the dynamical time-scale which is set by the Alfvén crossing time. For a magnetic field of 10^{14} G the Alfvén crossing time for the fundamental Alfvén oscillation is about 2 s. This value scales inversely proportional to the magnetic field.

5.1 Recovering purely shear oscillations of the crust

The purely shear oscillations for various realistic EoS in general relativity have been calculated for the linearized problem by Messios, Papadopoulos & Stergioulas (2001) and Sotani et al. (2007). To recover their results, we performed a series of simulations for a selection of models with zero magnetic field strength. As initial velocity perturbation we use a simple radial law in the form $v \approx \sin(\pi/2 * (r - r_{\rm cc})/(r_{\rm s} - r_{\rm cc}))$ multiplied by a sum of the first 10 vector spherical harmonics for the angular dependence. With this kind of perturbation we ensure to excite single modes with different values for the radial and angular mode numbers n and l. We evolve the system for 1 s in the case of $n = 0$ modes and 50 ms for the modes with $n \geq 1$. The resolution of the simulations was $120(r) \times 60(\theta)$ points in the domain $[0, r_{\rm s}] \times [0, \pi/2]$, the grid is equidistant in both directions and we used equatorial symmetry. The chosen grid corresponds to about 20 radial zones inside the crust.

Table 2. Frequencies of some torsional shear modes of the crust for different EoS. Numbers following the abbreviation of the EoS give the mass of the stellar model in solar mass units. The frequencies in round parenthesis are from Sotani et al. (2007), and the squared brackets give the result of the eigenmode analysis (see Appendix B). For the $n = 1$ and $n = 2$ modes we compare to the $l = 2$ case only. The frequencies of the eigenvalue calculation for $n = 0$ and $l > 2$ can be obtained by multiplying the corresponding frequencies for $l = 2$ with $\sqrt{(l-1)(l+2)}/2$. The error ranges shown in the table header correspond to the frequency spacing in the Fourier analysis.

Model	Mode frequency (Hz)						
	$n = 0$ (± 1 Hz)					$n = 1$	$n = 2$
	$l = 2$	$l = 3$	$l = 4$	$l = 5$	$l = 6$	(± 20 Hz)	
APR+DH 1.4	25.4 (24.6) [25.1]	40.0 (38.9)	53.6 (52.2)	67.3 (65.1)	80.0 (77.8)	741 (761) [734]	1190 (1270)
APR+DH 1.6	24.3 (23.4) [24.0]	38.5 (37.0)	51.2 (49.6)	64.3 (61.9)	76.5 (73.9)	829 (860) [825]	1340 (1430)
APR+DH 2.0	21.9 (21.3) [21.7]	34.6 (33.6)	46.3 (45.1)	58.0 (56.3)	69.2 (67.3)	1052 (1083) [1045]	1842 (1810)
L+DH 1.6	21.0 (20.6) [20.9]	33.1 (32.5)	44.8 (43.7)	55.6 (54.5)	66.8 (65.1)	565 (586) [567]	917 (980)
L+DH 2.0	19.5 (18.9) [19.2]	30.7 (29.9)	40.9 (40.2)	51.2 (50.1)	61.4 (59.9)	682 (713) [677]	1100 (1190)
APR+NV 1.6	23.9 (23.8) [23.6]	37.5 (37.6)	50.7 (50.5)	62.9 (63.0)	75.5 (75.3)	692 (689) [684]	1230 (1220)
APR+NV 2.0	21.5 (21.4) [21.2]	33.7 (33.9)	45.4 (45.5)	56.5 (56.7)	67.8 (67.8)	838 (858) [827]	1501 (1520)
L+NV 1.6	22.0 (21.8) [21.8]	34.7 (34.5)	46.8 (46.3)	58.6 (57.7)	69.7 (69.0)	526 (525) [522]	936 (930)
L+NV 2.0	19.5 (19.7) [19.6]	31.2 (31.1)	41.9 (41.7)	52.2 (52.1)	62.5 (62.2)	615 (615) [608]	1092 (1090)

Table 2 gives the oscillation frequencies of our dynamical simulations extracted from the Fourier analysis at points inside the crust. The frequencies of the modes agree up to a few per cent with those of the linear approximation (given in round parenthesis). For modes with $n \geq 1$, the frequency resolution of the Fourier transform does not allow us to resolve modes with the same n but different l, which are only separated from each other by a few Hz. Therefore, the measured frequency is a mixture of different l contributions, and its value is expected to be slightly larger than that of Sotani et al. (2007) for $l = 2$, which are reported in the Table 2 as well.

Additionally, we have computed the frequencies from the associated eigenvalue problem (Appendix B). For the computation of these frequencies we used a radial grid of about 80 zones in the crust. The results for the $n = 0$, $l = 2$ and $n = 1$ modes are given in squared brackets in Table 2. They agree up to a similar accuracy with those that have been obtained in the literature. To investigate the convergence properties of our code when no magnetic field is present, we have calculated the evolution of the $n = 0$ and $l = 2$ mode of our reference neutron star model for different grid resolutions: 180×60, 150×50, 120×40 and 90×30. The angular grid is equidistant, while the radial grid is equidistant only in the crust, where 40 per cent of the zones are located, and coarsens towards the centre of the star. The finer mesh in the crust ensures higher accuracy without significant increase of the computational costs. In order to save further computational power we assume equatorial symmetry. The mode frequencies extracted from the simulations at different resolutions agree within the frequency resolution of the Fourier transform. The upper panel of Fig. 2 shows the time evolution of the maximum amplitude of $\xi^{\varphi}_{,t}$ at the crust for different grid resolutions. One clearly sees that the numerical damping decreases with increasing resolution. For this simple test case it is possible to compute the order of convergence using the results for the three highest resolutions, when one assumes that the error in the interesting variable, f, scales as Δ^p, where Δ is the size of the numerical cell and p the order of convergence. To compute p one searches for roots of

$$\frac{f_{\rm coarse} - f_{\rm medium}}{f_{\rm medium} - f_{\rm fine}} = \frac{\Delta^p_{\rm coarse} - \Delta^p_{\rm medium}}{\Delta^p_{\rm medium} - \Delta^p_{\rm fine}}, \tag{55}$$

where the subscripts denote fine, medium or coarse grid resolution. The lower panel of Fig. 2 shows that after a short initial transient the order of convergence, p, rapidly converges to 2, which is the expected order of convergence of our numerical scheme.

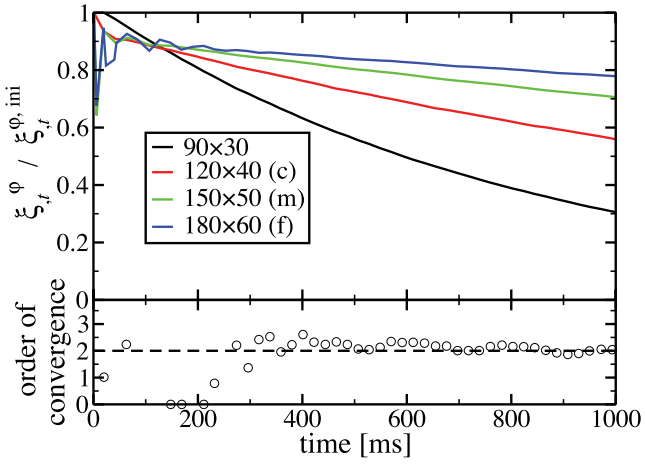

Figure 2. Numerical damping of crustal oscillations. The upper panel shows the evolution of the maximal amplitude of $\xi^{\varphi}_{,t}$ normalized to its initial value, at a point in the crust near the pole for different grid resolutions. The numerical damping decreases with increasing resolution. The lower panel shows the order of convergence (circles) computed using the three highest resolution simulations compared to the expected second-order convergence (dashed line).

5.2 Absorption of crustal shear modes by the Alfvén continuum

This subsection is concerned with the absorption of purely shear modes of the crust into the Alfvén continuum of the core. We will often refer to this process as the *damping* of crustal shear modes. This expression may mislead the reader to think of dissipation processes. However, damping in the current context refers to the transfer of energy from crustal modes into the continuum of the core, but not to dissipation of energy. Only when referring to numerical damping we mean the usual concept describing the loss of ordered kinetic energy by numerical dissipation.

5.2.1 $n = 0$ *shear modes*

As we have shown in Gabler et al. (2011) purely shear oscillations are absorbed very efficiently by the Alfvén continuum of the core for magnetic field strengths $B \gtrsim 5 \times 10^{13}$ G. In this case the amplitude of the perturbations of the crust is damped by transferring their energy to the Alfvén continuum. To analyse how this damping scales with the magnetic field strength, we have performed a series of simulations for different crustal modes with $n = 0$, $l \geq 2$ for different magnetic fields (0, 10^{13}, 2×10^{13}, 5×10^{13}, 8×10^{13}, 10^{14} and 2×10^{14} G). For these simulations we use a grid of 150×100 zones covering a domain $[0, r_s] \times [0, \pi]$, which is equivalent to the medium grid of the previous section but not assuming equatorial symmetry. Here, we use the solution of the eigenvalue problem for the unmagnetized crust (see Appendix B) as initial perturbation for the velocity. Symmetries are exploited whenever a perturbation is purely symmetric or antisymmetric with respect to the equatorial plane.

In the following we will discuss our results by using so-called overlap integrals (derived in Appendix B). These overlap integrals are the expansion coefficients of an arbitrary spatial function in the basis of the crustal oscillation eigenmodes, i.e. they give a measure of how strong the different eigenmodes are excited (see Gabler, Sperhake & Andersson 2009, for an application to radial oscillations of neutron stars). In Fig. 3 we show the time dependence of the maxima of the overlap integrals defined in equation (B11) corresponding to the $n = 0$, $l = 2$ crustal mode for different magnetic field strengths. The stronger the field is, the faster the damping of the shear mode proceeds. For high field strength, $B > 2 \times 10^{14}$ G, it is not possible to obtain a characteristic damping time τ, because the time-scale is shorter than one oscillation period. Therefore, the latter can be used as an upper bound for τ. For 2×10^{14} G we show the evolution of the overlap integral only up to the time when global magnetoelastic oscillations start to dominate and interfere with the purely shear modes of the crust.

Table 3 shows the damping time-scales, obtained by analysing the overlap integrals, for different $n = 0$, $l \geq 2$ modes and different magnetic field strengths. The values for zero magnetic field serve as a measure of the numerical damping of the code. As expected for numerical dissipation processes, modes with higher l suffer stronger from numerical damping than lower l (see also Cerdá-Durán 2010). For weak magnetic fields, e.g. 10^{13} G, the damping of high l modes is dominated by numerical dissipation, while for low l modes it is caused by the interaction with the Alfvén continuum of the core. For magnetic fields stronger than 5×10^{13} G, we are confident that the damping time of all studied modes is physical and not due to numerical dissipation. Above 2×10^{14} G the oscillations are damped on shorter time-scales than the respective oscillation period, and hence it is impossible to obtain accurate damping times.

Table 3. Damping time-scale τ in ms for different $n = 0$, crustal shear modes for different magnetic field strengths.

Magnetic field (G)	τ (ms) for mode $n = 0$						
	$l = 2$	$l = 3$	$l = 4$	$l = 5$	$l = 6$	$l = 7$	$l = 8$
0	1130	1110	1030	874	654	466	313
1×10^{13}	688	835	846	764	599	441	302
2×10^{13}	102	287	478	534	481	385	279
5×10^{13}	83	85	72	54	38	63	104
8×10^{13}	58	60	43	38	37	34	28
1×10^{14}	46	48	37	38	40	33	27
2×10^{14}	20	21	21	23	19	21	21

Fig. 4 shows τ/t_A, where t_A is the Alfvén crossing time of the star at the pole. The damping time of crustal modes due to the absorption by the Alfvén continuum scales linearly with t_A, i.e. τ decreases with increasing magnetic field. The mean damping time is about $0.04\, t_A$. Deviations from this value (see Fig. 4) depend non-trivially on the magnetic field and the mode number l. The spread decreases with increasing magnetic field strength, being smallest for our $B = 2 \times 10^{14}$ G simulation. Low l modes (filled circles in Fig. 4) show a smaller spread around the mean value than the higher l modes (crosses in the same figure).

These deviations are expected, because the damping depends on a variety of parameters as for example the frequency of the crustal mode, the frequencies available in the Alfvén continuum of the core

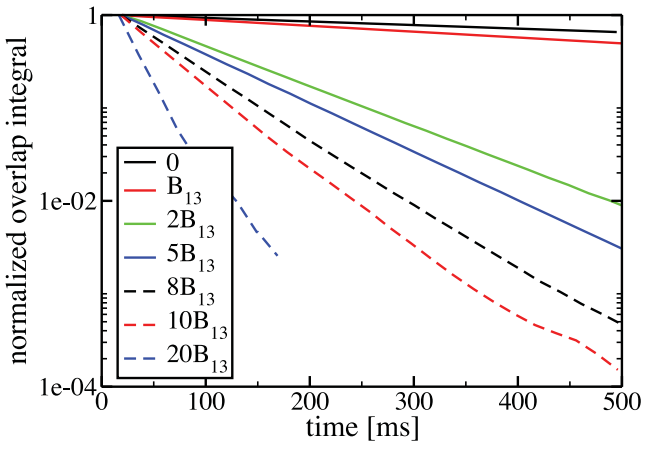

Figure 3. The maximum of the normalized overlap integral for the $n = 0$, $l = 2$ eigenmode of the crust as a function of time. Stronger magnetic field results in faster damping of the initially excited crust mode. Orthogonality of different eigenmodes is fulfilled numerically up to about 10^{-5}. In the legend we introduced the abbreviation $B_{13} = 10^{13}$ G.

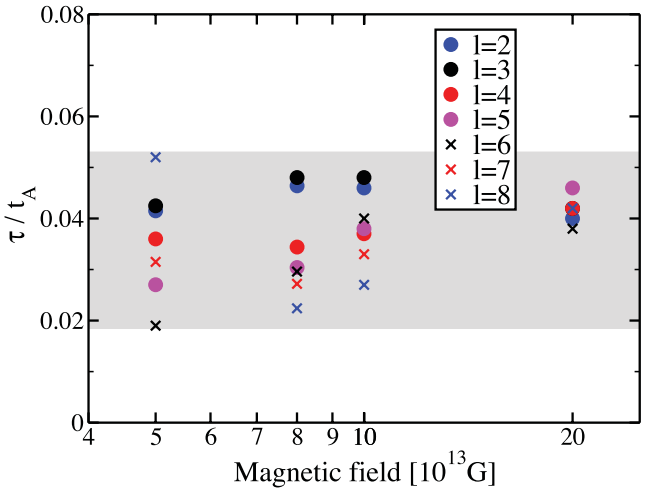

Figure 4. The dependence of τ/t_A on the magnetic field. The stronger the magnetic field is the less is the spread of the numerical values for different l around this value. The shaded area indicates the maximum range of variation of τ/t_A around the mean value (~0.04).

and the spatial structure of the crustal modes. Numerical effects may also affect the damping times. First, the grid resolution necessary to obtain a comparable accuracy for different modes increases with increasing mode number l. Secondly, waves in the crust reaching the core–crust interface will propagate into the core as Alfvén waves. Because of the jump in the wave velocity at the interface, the wavenumber increases, i.e. the resolution requirements in the core are more restrictive. This holds, in particular, for weak magnetic fields, where the jump in the wave velocity is larger, and for large l modes with higher frequencies.

The damping time at a given magnetic field strength $B > 10^{13}$ G varies only by at most a factor of 2 between different l, but may vary significantly with the magnetic field strength. This indicates that the damping is dominated by the magnetic field and does not depend sensitively on the mode structure itself, i.e. there will always be a part of the continuum that is able to drain the energy from the crustal oscillations.

A more detailed discussion of the damping of the different crustal modes is beyond the scope of this work. Our results do not favour a crustal-mode interpretation of the observed QPOs in SGRs, because any crustal shear mode is damped sufficiently fast for magnetic field strengths well below the typical magnetar field strengths $\sim 5 \times 10^{13}$ G. Although there might exist SGRs with weaker magnetic fields (Rea et al. 2010), QPOs have only been observed so far in magnetars with the strongest fields.

5.2.2 $n > 0$ *shear modes*

The higher radial overtones ($n > 0$) of the shear modes have frequencies above 500 Hz (see Table 2) and are usually used to explain the QPOs of SGR 1806−20 with the highest frequencies of 625 and 1840 Hz. As these modes have at least one node inside the crust computing their evolution demands much higher spatial resolution than necessary for the $n = 0$ modes. Thus, it was practically impossible for us to follow their evolution over several Alfvén crossing times to the same accuracy as for the $n = 0$ modes. However this would have been necessary to draw more reliable conclusions about damping times or interaction of these modes with the Alfvén continuum in the core. Nevertheless, we can make some qualitative statements.

The time needed for a shear wave ($v_S \sim 1000\,\mathrm{km\,s^{-1}}$) to travel through the crust ($\Delta r_{\mathrm{crust}} \sim 1$ km) corresponds to the inverse of the frequency of the first overtone ($n = 1$), which is of the order of $f \sim 1$ kHz. Assuming that the wave travels inside the crust along the θ-direction (travel path $\Delta r \sim 10\pi$ km), a similar estimate results in frequencies $v_S/\Delta r \sim 30$ Hz which is of the order of the frequency of the fundamental $n = 0$ oscillation. Therefore, we may conclude that the $n = 0$ modes represent waves that travel predominantly parallel to the crust–core interface, while the $n = 1$ modes correspond to waves that travel radially. This may explain the strong dependence of the $n = 0$ modes on the angular number l and the weak dependence of the $n = 1$ modes (see Table 2 with the corresponding discussion, and Sotani et al. 2007). Hence, we expect the $n = 0$ modes, derived with isotropic shear modulus, to be much more affected by the presence of an anisotropic magnetic field than the $n = 1$ modes. In particular, near the equator where the coupling between the crust and the core is weaker than close to the pole (see equation 42) the shear waves may travel back and forth in the crust without interacting strongly. Additionally, at the equator the magnetic field is almost parallel to the θ-direction, i.e. the direction of the Alfvén waves is perpendicular to the direction

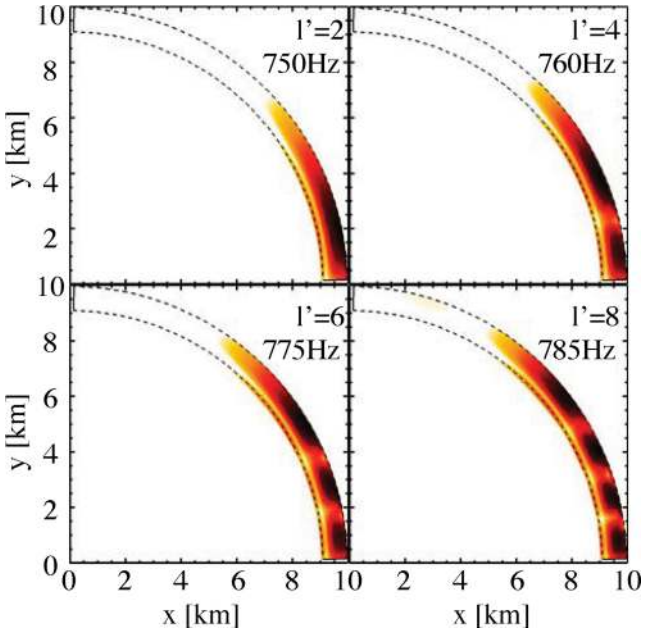

Figure 5. The spatial structure of the first $n = 1$, antisymmetric crustal shear modes in the presence of a moderate magnetic field of 5×10^{14} G. The oscillation patterns are strongly distorted from the typical l-dependence of the spherical harmonics and only exist in regions close to the equator, where the coupling between the core and the crust is weakest. We therefore label their angular dependence with l'. The dashed lines indicate the region of the crust and the colour scale ranges from white (minimum) to red-black (maximum).

of the $n = 1$ shear waves. This suggests that the $n = 1$ shear waves are not influenced strongly by the presence of moderate magnetic fields ($\lesssim 10^{15}$ G). According to these theoretical considerations we expect the overtones of the shear modes to survive longer than the $n = 0$ modes.

To investigate this issue, we have performed two simulations with our reference model at magnetic field strengths of 2×10^{14} and 5×10^{14} G. The resolution for antisymmetric simulations ($l = \{2, 4, 6, \ldots\}$) was 150×50 zones. The initial perturbation consisted of the $n = 1, l = 2$ mode of the crust only. In Fig. 5 we show the main contributions to the oscillations as obtained by Fourier analysing the time evolution of the simulation with 5×10^{14} G. The QPO patterns are compressed towards the equator and strongly distorted from the typical l-dependence of spherical harmonics of the purely shear eigenmodes of the crust (see Appendix B). To account for this difference we label these QPOs with l'. Naturally, the initial data of the undistorted l mode excites many distorted l'-QPOs. As expected from the theoretical considerations above, the strongest amplitudes of the oscillations appear near the equator, where the coupling to the core is weakest (see Fig. 5). The magnetic field also increases the spacing between the frequencies of successive $n = 1$, l' modes from $\Delta f \approx 1$ Hz without field to $\Delta f \approx 10$ Hz (see Sotani et al. 2007, for a discussion of purely shear eigenmodes).

To study the behaviour of the different QPOs, we calculate the corresponding overlap integrals (equation B11) but taking the spatial structure obtained from the Fourier analysis (Fig. 5) as basis functions. The time evolution of the maxima of these overlap integrals for $l' = \{2, 4, 6, 8\}$ can be seen in the left-hand panel of Fig. 6. Indeed all of l'-QPOs are excited by the purely shear $n = 1$,

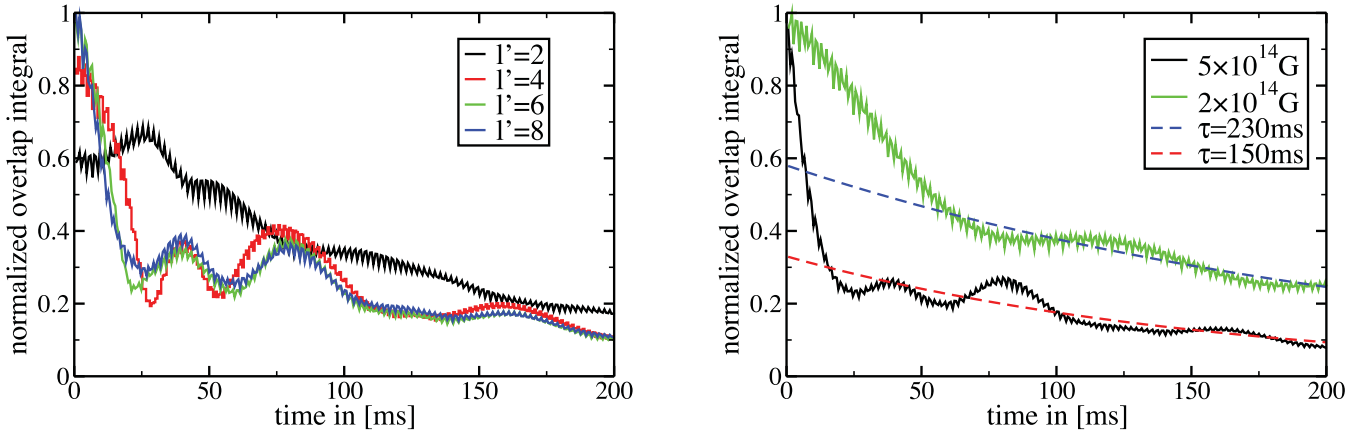

Figure 6. Left-hand panel: the normalized overlap integrals of the evolution for the first few $n = 1$, antisymmetric magnetoelastic modes at $B = 5 \times 10^{14}$ G. The approximate mode structure is taken from the Fourier analysis (see Fig. 5). Strictly speaking there are no modes in terms of the result of the linear analysis, but the influence of the magnetic field is insufficient to destroy the coherent oscillations in all parts of the crust. The initial perturbation of the $n = 1$, $l = 2$ crustal mode excites a large number of the magnetoelastic modes which are all damped on a time-scale of ∼150 ms. Right-hand panel: the overlap integral performed for a basis with purely radial dependence $\Xi_i(r, \theta) = R_{\lambda_r}$ (see Appendix B) of the $n = 1$ modes. These integrals are a measure of how strong the ensemble of all l', $n = 1$ modes is excited. The damping time, indicated by the fits to an exponential (dashed lines), for 2×10^{14} G (5×10^{14} G) of $\tau = 230$ ms (150 ms) is much longer than that of the $n = 0$ modes, which is of the order of several ms only.

$l = 2$ eigenmode perturbation. Since the frequencies of the different $n = 1$ modes are very similar, i.e. hard to disentangle in any analysis of the simulations, we average all $n = 1$ modes to estimate the total damping time of the $n = 1$ QPOs. To this end we calculate the overlap integral with the radial function $\Xi_i(r, \theta) = R_{\lambda_r}$ corresponding to the pure shear eigenmodes obtained with equation (B8). This effectively averages over the angular dependence, and provides a measure of how strong the ensemble of all l', $n = 1$ QPOs is excited. The corresponding plots for $B = 2 \times 10^{14}$ and 5×10^{14} G are shown in the right-hand panel of Fig. 6. As indicated by the fitting functions with damping times of 150 and 230 ms, the damping time-scale of the $n = 1$ QPOs is much longer than for the $n = 0$ modes at the given magnetic field strength of a few 10^{14} G.

However, one has to be very cautious at this point. With the resolution used here, we are not able to resolve the Alfvén oscillations inside the core of the neutron star which could damp the crustal shear oscillations resonantly. At 5×10^{14} G the fundamental Alfvén oscillation is about 2 Hz. To resolve the resonant coupling to the crustal $n = 1$ mode of roughly 500 Hz one would need the 250th overtone. Simulations with appropriate grid resolution would take of the order of years. For the damping process itself this lack of resolution should not be a problem, because the numerical method employed should take all necessary information into account, i.e. the Riemann solver at the crust core interface considers all the local information of possible waves travelling into the core. The problem arises inside the core, where a low resolution leads to an averaging out of all fine-scale structure. Hence, the energy of the Alfvén overtones of the continuum is transformed to resolved low-order oscillations, i.e. we cannot trust the oscillations inside the core. However, as long as the Alfvén oscillations do not reach the crust at the opposite side of the star at $t \approx t_A = 0.5/f_A = 1.2$ s (for $B = 5 \times 10^{14}$ G), a simulation of the crust region should give correct results. Therefore, the present estimate of the damping time of the $n = 1$ overtones should be considered as a lower limit, because the main effect we are missing is the excitation of crustal magnetoelastic QPOs by incoming Alfvén oscillations of the core.

5.2.3 *Results for different equilibrium models*

All previous results were obtained for a model based on the APR+DH EoS and a mass of 1.4 $M_\odot$. Simulations using other EoS or different masses for the equilibrium model yield qualitatively similar results.

In table 2 of Gabler et al. (2011) we showed that the damping of purely crustal shear modes occurs on the order of 100 ms or less for a variety of EoS and masses at a magnetic field strength of $B = 10^{14}$ G. The initial models that we used in those simulations employed a different prescription for the internal energy (ideal gas) than the values provided in the EoS tables. As these models were thus thermodynamically inconsistent, we have recomputed them with the appropriate internal energy values. The resulting damping times are at most 20 per cent longer than the values reported in Gabler et al. (2011). Some of the corrected damping times are shown in Table 4. The conclusions drawn in Gabler et al. (2011) are not affected at all by this change, because the maximal damping time is still less then 100 ms in all cases. The variation of the damping times with the EoS at a given magnetic field is not surprising. The relative size of the crust of these models varies roughly by a factor of 3 (see Sotani et al. 2007), and the shear modulus of both crustal EoS is of comparable size. This explains the smallness of the observed variations in Gabler et al. (2011) which do not exceed a factor

Table 4. Damping time-scales τ due to resonant absorption of crustal shear modes by the Alfvén continuum for initial perturbation modes $l = 2$, 3 and 9 for different combinations of EoS at $B = 10^{14}$ G. The number in the labelling of the EoS represents the mass of the neutron star model in $M_\odot$.

EoS	τ (ms) at $B = 10^{14}$ G		
	$n = 0, l = 2$	$n = 0, l = 3$	$n = 0, l = 9$
APR+DH 1.6	45	47	21
APR+DH 2.0	38	41	17
L+DH 1.6	57	61	27
L+DH 2.0	52	56	25

of 5. A significantly lower shear modulus, as proposed in Steiner & Watts (2009), would lead to even shorter damping times of the crustal shear modes.

The influence of the details of the EoS is not substantial because when trying to explain the frequencies of the QPOs observed in SGRs as shear oscillations, the shear modulus should lie in the range we use in this work. Otherwise it is already impossible to reproduce the correct range of frequencies within the crustal oscillation model. Changing the shear modulus somewhat would have only a modest effect on the damping times. However, even for a hypothetically exotic shear modulus, which could be one order of magnitude larger than the actual values we use, the crustal shear oscillations would be damped much too fast to explain long-lived QPOs. We therefore argue that we can safely exclude shear oscillations as a viable explanation of observed magnetar QPOs, for the magnetic field configurations studied here.

5.3 QPO structure for intermediate field strength

In Gabler et al. (2010, 2011) we have shown that the crust significantly changes the structure of the QPOs for intermediate magnetic field strengths between 5×10^{13} and 10^{15} G compared to models without crust. In this section we investigate the behaviour of the Alfvén QPOs of the core in this regime further.

5.3.1 QPO structure at 4×10^{14} *G*

In this subsection we will analyse the results of two simulations with a resolution of 100×40 zones and computational domain $[0, r_s] \times [0, \pi/2]$. We perform one simulation with $l = 2$ initial data and antisymmetry with respect to the equatorial plane, and another symmetric one with $l = 3$ initial data. Both runs were evolved up to $t \approx 5$ s.

For the model APR+DH 1.4 with a magnetic field strength of $B = 4 \times 10^{14}$ G we find three different families of QPOs. Following Cerdá-Durán et al. (2009) we label the *lower* QPOs as $L_n^{(\pm)}$ and the *upper* QPOs as $U_n^{(\pm)}$. A new family of QPOs appears, which we call e.g. QPOs and label them as $E_n^{(\pm)}$. To avoid confusion with the previous work of Cerdá-Durán et al. (2009), and because the fundamental upper symmetric QPO has special properties as we will show below, it will be labelled as $U_*^{(+)}$ at low magnetic field strength. The plus and minus sign in the description of the QPOs indicate symmetry (+) or antisymmetry (−) of the QPO with respect to the equatorial plane.

In Fig. 7 we plot the distribution of the Fourier amplitude inside the star. Lower QPOs, as shown in panels (a) and (b), are attached to field lines which close inside the core. In contrast, upper QPOs are located closer towards the magnetic poles at open field lines (panels c–f). A third family, the edge QPOs, is connected to the open field line inside the core of the neutron star which just fails to close inside (last open field line). These QPOs can be seen in panels (g)–(i) of Fig. 7. The two QPOs $U_1^{(+)}$ and $E_4^{(+)}$ have very similar frequencies. Because of limited evolution time and hence limited resolution for the Fourier transform both QPOs contribute significantly to the Fourier signal at the corresponding frequency as can be seen in panel (i). Similarly, the figure for $E_3^{(+)}$ contains some contribution of $U_0^{(+)}$ along the field lines crossing the equator between a radius of 1 and 4 km. In both panels the edge QPOs are concentrated on the field lines which cross the equatorial plane at around 5 km. The naming of the edge QPOs becomes clearer in Fig. 8, where we plot the Fourier amplitude of the velocity, averaged per field line in the frequency–radius plane. The maxima indicate the position of the QPOs. The red and green lines are the continuum of frequencies obtained with the semi-analytic model introduced in Cerdá-Durán et al. (2009) and adopted here to the problem in the presence of the crust.

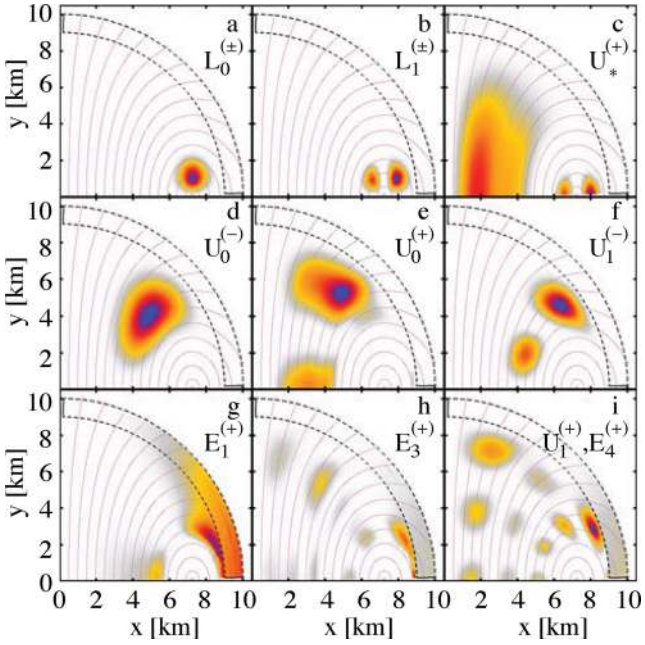

Figure 7. The Fourier amplitude inside the neutron star for the model APR+DH 1.4 at $B = 4 \times 10^{14}$ G. Shown are the first two lower QPOs $L_0^{(\pm)}$ and $L_1^{(\pm)}$, the first four upper QPOs $U_*^{(+)}$, $U_0^{(-)}$, $U_0^{(+)}$ and $U_1^{(-)}$ and some selected edge QPOs $E_1^{(+)}$, $E_3^{(+)}$ and $E_4^{(+)}$. (The figure for $E_2^{(+)}$ was not very clear due to contamination with other QPOs.) The plus and minus sign indicate symmetry (+) and antisymmetry (−) with respect to the equatorial plane. Magenta lines indicate magnetic field lines, and black, dashed lines the location of the crust. The colour scale ranges from white-blue (minimum) to red-black (maximum).

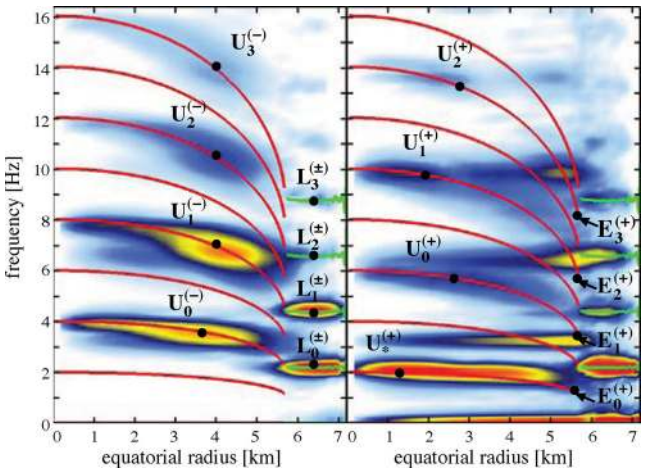

Figure 8. The averaged Fourier amplitude along different magnetic field lines labelled by the radius where they cross the equator for model APR+DH with $M = 1.4\,M_\odot$ and $B = 4 \times 10^{14}$ G. Red and green lines give the Alfvén continuum obtained with the semi-analytic model. The locations of the QPOs are indicated by black dots. Left-hand panel: antisymmetric simulation; right-hand panel: symmetric simulation. The colour scale ranges from white-blue (minimum) to orange-red (maximum).

The different families of QPOs mentioned above and shown in Fig. 7 can also be identified in Fig. 8. The lower QPOs are attached to the closed field lines which cross the equatorial plane near 6.5 km. Since they are connected to the closed field lines these QPOs do not have a preferred symmetry, and hence are present in symmetric and antisymmetric simulations. The continuum of frequencies derived with the semi-analytic model (green lines in Fig. 8) has a minimum at the point where we find the lower QPOs. We thus interpret the $L_n^{(\pm)}$ as turning point QPOs (see Levin 2007). With the exception of the fundamental $U_*^{(+)}$, which is located almost at the turning point of the semi-analytic model, the upper QPOs are localized in the continuum of the open field lines (red lines in Fig. 8) that cross the equatorial plane at 2–4 km.

The members of the new family of QPOs, also obtained in Colaiuda et al. (2009), are called edge QPOs because of their position in Fig. 8. These QPOs are related to those parts of the continuum, obtained with the semi-analytic model (red lines), which do not connect to the continuum of the closed field lines (green lines) (see also the sketch in Fig. 1). For more details on the interpretation of the QPO structure without crust we refer to Cerdá-Durán et al. (2009) and with crust to Gabler et al. (2010).

5.3.2 *Differences caused by the presence of the crust*

The lower QPOs attached to the closed field lines are reproduced qualitatively similar as in the case without crust. The only difference is that they are limited to the field lines which close inside the core and do not extend into the crust.

However, the upper QPOs which are located near the pole in models without crust (Sotani et al. 2007; Cerdá-Durán et al. 2009; Colaiuda et al. 2009) can now be found at substantial distance from the poles, i.e. at lower latitudes (see also fig. 4 in Gabler et al. 2011). In simulations without crust the oscillations were associated with the maximum at the turning point of the continuum at the pole, while if the crust is included, we obtain the maximal amplitudes away from the pole and inside the continuum predicted by the semi-analytic model in the absence of a crust. One possible interpretation of this new feature is that the shear modulus in the crust alters the propagation of magnetoelastic oscillations in the region near the pole in such a way that standing waves cannot form at all along individual field lines or, if they form, they go quickly out of phase with nearby field lines in this region.

At this point it is helpful to recall the problem of the reflection of plane-parallel waves, where the reflection coefficient depends on the jump in the propagation velocity or equivalently on the index of refraction. The stronger the jump in the index is, the larger is the fraction of the incident wave which becomes reflected. Using this analogy we would expect that the smaller the difference in propagation velocity at the crust–core interface is, the more refraction into the crust should occur and less reflection back into the core should be produced. If significant refraction into the crust occurs, no stable standing waves can be maintained during the evolution. When following the crust–core interface from the pole towards the equator the coupling between crust and core becomes weaker, see equation (42) where the θ dependence of the coupling factor is realized in b^r. The magnetic field in the radial direction, and hence the Alfvén velocity, decreases with increasing θ. Therefore, the jump in the propagation velocity increases, and thus the fraction of the wave which is reflected will also increase along this trajectory. For sufficiently low magnetic fields there should always be a region near the equator were almost perfect reflection occurs. However, when following the crust–core interface from the equator towards the pole, one will reach a characteristic magnetic field strength where insufficient reflection occurs to maintain stable standing waves along a certain field line. At this point we find the maximum amplitude of the QPO in the presence of a crust. We will investigate the reason for this behaviour further in Section 5.3.4.

The new position of the maximum amplitude of the QPOs is thus determined by two effects. Near the pole the magnetic field lines get out of phase due to the interaction through the extended crust, because a significant fraction of the oscillation is refracted. The magnetic field lines can be seen like strings which are not attached to a rigid but rather 'moving' boundary, i.e. the crust which responds to the oscillations. The resulting effect is a strong coupling of different magnetic field lines and, consequently, an energy transfer between the lines due to the scalar shear modulus. In this region and for magnetic field strengths studied here, each field line seems to act as a damped oscillator. Near the equator the magnetic field lines get out of phase due to phase mixing like in the case without extended crust. The additional damping close to the pole makes the corresponding upper QPOs to be shorter lived than in the case without crust. This effect can be observed in the right-hand panel of Fig. 9, where we show the magnetic plus the kinetic energy per field line divided by the total magnetic plus kinetic energy at the given time as a function of time for different field lines. The initially excited QPOs attached to the field lines between 4.5 and 5 km disappear rapidly after about 0.5 s. In contrast, the lower QPOs and the fundamental symmetric QPO near the pole persist during the whole evolution. Fig. 9 may suggest that the lower QPO gain energy with time. However, this apparent energy increase is not a physical effect, because the total energy decreases with time due to numerical dissipation. Hence, the relative amplitudes of the energy of the lower QPOs increase, while their absolute amplitude decrease slightly because of numerical dissipation.

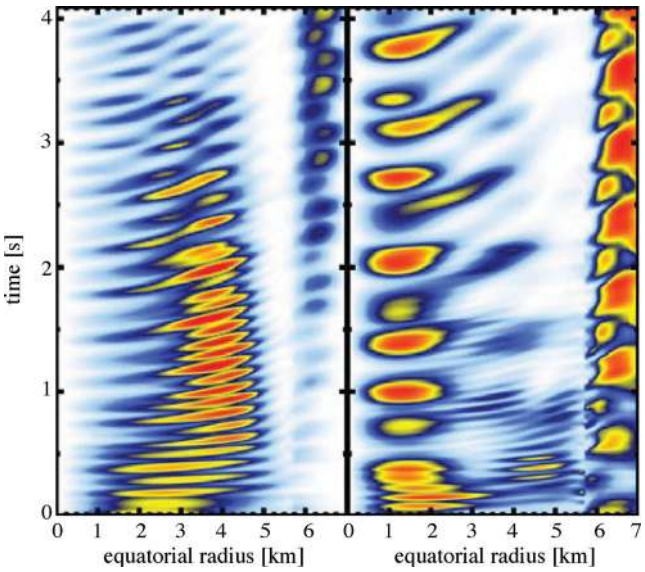

Figure 9. Evolution of the magnetic plus kinetic energy per field line divided by the sum of the energy over all field lines. The field lines are labelled by their crossing point with the equator. Note that as the total energy decreases with time the apparent increase of the energy of the lower QPOs is due to colour rescaling at every time-step. Their amplitude actually decreases, but more slowly than that of the upper QPOs. The left-hand panel shows antisymmetric and the right-hand panel symmetric simulations. The colour scale ranges from white-blue (minimum) to orange-red (maximum).

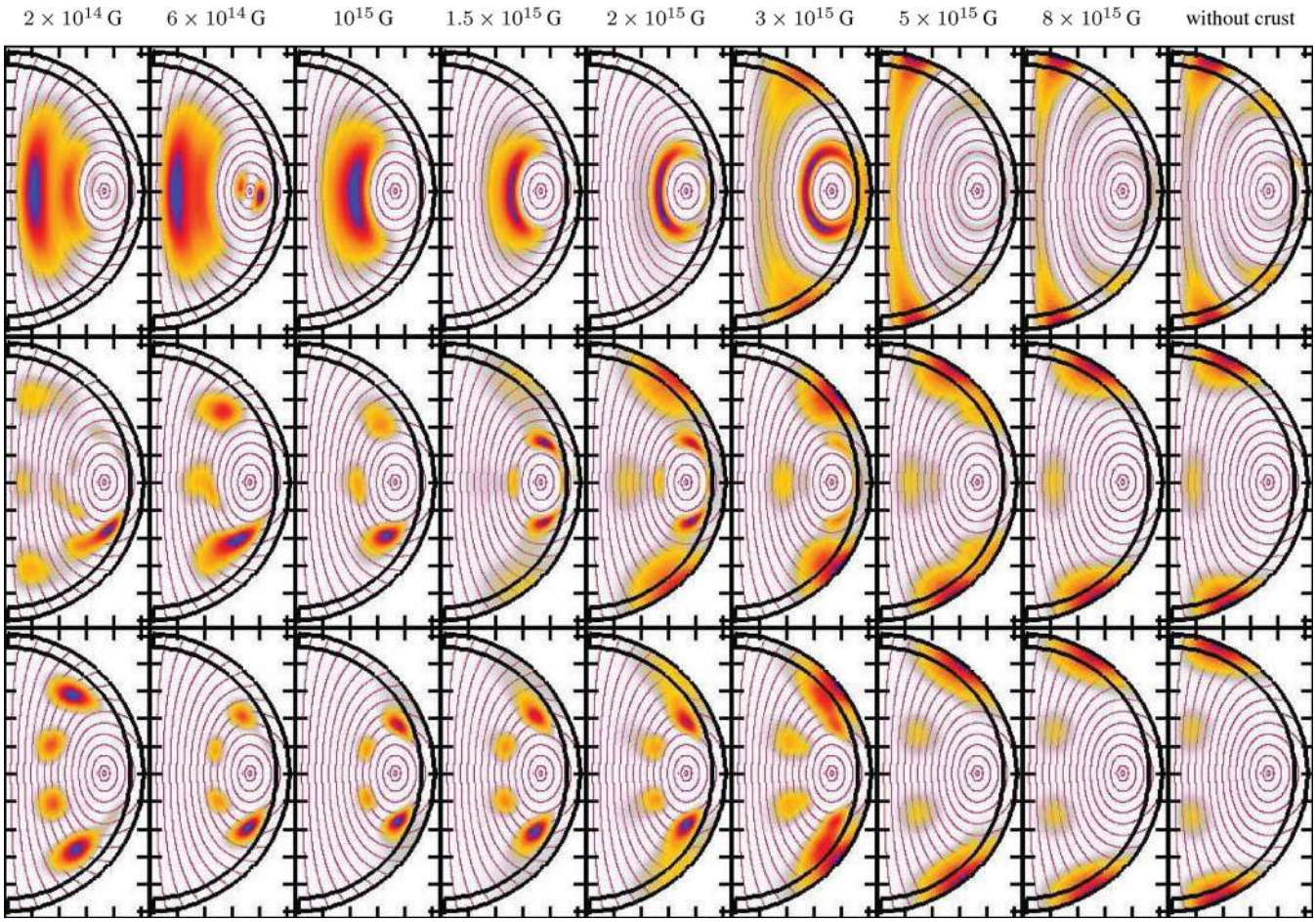

Figure 10. Structure of upper QPOs at different magnetic field strengths for the model APR+DH 1.4. The panels show the fundamental symmetric $U_*^{(+)}$ (upper panels), the symmetric $U_0^{(+)}$ (middle panels) and antisymmetric $U_1^{(-)}$ QPOs (lower panels). The frequencies of the QPOs shown here are given in Table 5. The colour scale ranges from white-blue (minimum) to red-black (maximum).

Compared to simulations without crust (Cerdá-Durán et al. 2009) we find a new fundamental upper QPO $U_*^{(+)}$. This QPO appears because the boundary condition at the crust–core interface causes a reflection which results in a node at this surface. Without crust the boundary condition at the surface of the star implies a maximum there and the fundamental oscillation has the node at the equator in this case. Therefore, the symmetric QPO $U_0^{(+)}$ must have an additional node inside the core (see panel e in Fig. 7 or the second row of Fig. 10). $U_*^{(+)}$ situated between 1 and 2 km (Fig. 9, the right-hand panel) decays less rapid than the other upper QPOs, $U_0^{(-)}$, $U_{n\geq 0}^{(+)}$ and $U_{n>0}^{(-)}$. This may be related to the fact that at $B = 4 \times 10^{15}$ G, $U_*^{(+)}$ is located close to the maximum of the continuum (see Fig. 8). There the gradient of the continuum is less steep, and neighbouring field lines get out of phase less rapidly. This behaviour is similar to a turning point QPO, which persists for longer time than edge QPOs (Levin 2007).

5.3.3 Changing QPO position with increasing magnetic field

For magnetic field strengths between 10^{14} and 10^{15} G the simulations reveal that the location of the upper QPO, $U_n^{(\pm)}$ changes within the neutron star. This was not observed in the case of pure Alfvén oscillations in Cerdá-Durán et al. (2009) or Sotani et al. (2008b), where the upper QPOs were always observed close to the pole. Fig. 10 (first three columns) shows the new effect, where we plot the spatial structure of the Fourier amplitude of the QPOs. When increasing the magnetic field from 2×10^{14} to 10^{15} G the upper QPOs $U_n^{(\pm)}$ move from a location near the pole towards the equator. The change in position of the $U_n^{(\pm)}$ is shown in Fig. 10 only for $U_0^{(+)}$ and $U_1^{(-)}$, but holds for all higher overtones as well and does not depend on the symmetry. For the fundamental $U_*^{(+)}$ the dislocation is less (upper row in Fig. 10). One can understand this behaviour at least partially with the help of the semi-analytic model. Fig. 8 shows that the frequencies and the symmetry of the QPOs are correctly predicted, if we assume that the Alfvén wave is reflected at the crust–core boundary. However, the semi-analytic model cannot explain where within the continuum the QPOs are situated.

Remembering the analogy with the reflection of plane-parallel waves in the preceding subsection and bearing in mind that with increasing magnetic field b^r the relative jump in the propagation velocity on both sides of the crust–core interface at a given position θ decreases, more parts of an incident wave get refracted into the crust. This means that the point where stable standing waves can be maintained should move towards the equator. This is exactly confirmed in Fig. 10, where for magnetic fields $\lesssim 10^{15}$ G the QPOs move from close to the pole towards the equator, as the magnetic field strength increases.

5.3.4 *Reflection of pulses and spread in crust*

In the absence of an elastic crust, Alfvén wave packets are supposed to travel approximately along magnetic field lines, as the characteristic direction of propagation of any magnetic perturbation coincides with the direction of the magnetic field. However, when a crust is added this picture changes. The direction of propagation of magnetoelastic waves no longer coincides with the magnetic field direction (compare the different eigenvalues in this case given in equation 31). One would therefore expect a perturbation, travelling along magnetic field lines from the centre of the star towards the surface to spread out past the crust–core interface. Such a spread is strong for low magnetic field strengths, when the isotropic shear modulus dominates in the crust region and weak for high magnetic field strengths, when the opposite is true. This behaviour is shown in Fig. 11, where we display the renormalized sum of the kinetic and magnetic energy per field line for simulations at 5×10^{14} G. The initial perturbation is restricted to a limited region of the star about 4 km above the equator. The left-hand panels show the expected behaviour for a pulse which travels along a field line with no crust present. Two initial perturbations differing only by the location of the star get reflected at the surface and travel back towards the centre. Any deviations from travelling perfectly along the initially excited field lines is caused by a numerical coupling of different field lines and the very weak coupling through the boundary condition at the surface of the star. Taking a crust into account but imposing the same initial perturbations the wave packets are spread whenever entering the crust, which happens at around 70 ms for the first time, and subsequently after about every 130 ms (right-hand panels). For initial data located at field lines crossing the equator around 2 to 3 km (lower right-hand panel), the spread is more drastic. After some reflections there are phases (around 700 and 850 ms), when no significant perturbation amplitudes can be found around the field lines which initially carried the perturbation.

However, the scenario of an initially localized wave packet considered here cannot rule out the existence of standing waves along individual field lines. Nevertheless, it suggests that additional effects may be introduced by the spreading of wave packets in the crust which probably change the Alfvén continuum of our semi-analytic model, where one assumes standing waves which get reflected at the crust–core interface (or at the surface for stronger magnetic fields).

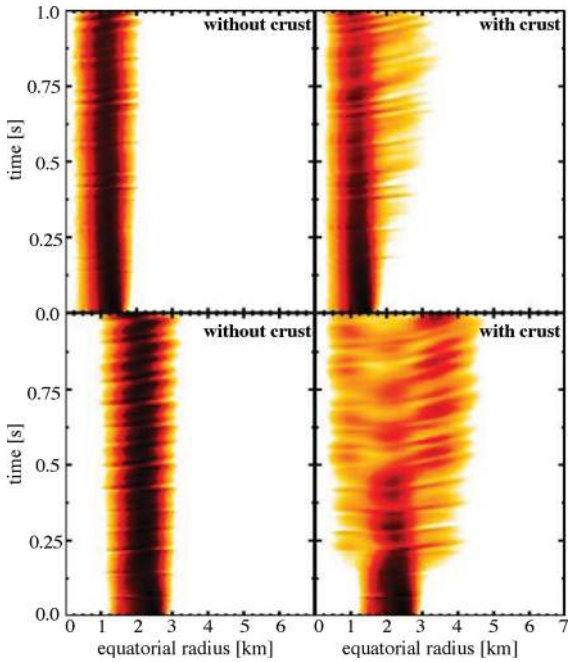

Figure 11. Evolution of the magnetic plus kinetic energy per field line divided by the sum of the energy of all field lines for the model APR+DH 1.4. The field lines are labelled by their crossing point with the equator. The pulse reaches the surface at around 70 ms for the first time and the crossing time is about 130 ms. Left-hand panels: simulation without crust; right-hand panels: simulation including crust. The upper and lower panels differ by the location of the initial perturbation. Colour scale ranges from white (minimum) to red-black (maximum).

5.3.5 *Conservation of angular momentum*

Analysing the convergence properties of our numerical simulations in the intermediate magnetic field case is more complicated because the contributions to the stress–energy tensor from the magnetic field and the shear are of the same order of magnitude. The two extreme regimes have been tested above (purely shear oscillations) or in Cerdá-Durán et al. (2009) (purely Alfvén oscillations). In the present approach, the total angular momentum $J_{\rm tot} \equiv \int S_\varphi \, {\rm d}V$ is the only globally conserved quantity, with ${\rm d}V = \sqrt{\gamma}\, {\rm d}r\, {\rm d}\theta\, {\rm d}\phi$. We do not expect conservation of the energy of the perturbation in our simulations, because neglecting the coupling to poloidal oscillations and assuming purely poloidal magnetic fields, renders the deviations of the total energy from the energy of the unperturbed background configuration to be of second order in the perturbations, while our approach is accurate to first order.

The total angular momentum $J_{\rm tot}$ should be conserved inside the computational volume, but the boundary condition we have chosen (see Section 2.3) allows for non-vanishing flux through the surface. As we chose initial perturbations with the angular dependence of the vector spherical harmonics the angular momenta in both hemispheres cancel by construction and the total angular momentum of the star is zero. For antisymmetric perturbations the losses/gains through the surface cancel, respectively, while for symmetric perturbations there remains a non-zero contribution. Fig. 12 shows the variation of the total angular momentum during the evolution for an symmetric simulation with $l = 3$ initial data at three

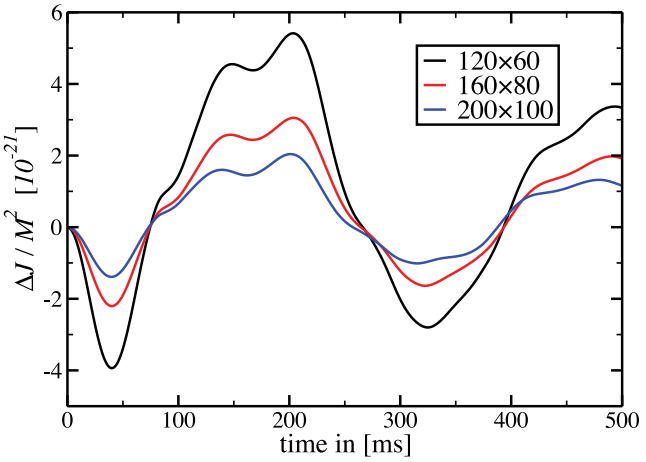

Figure 12. Variation of the total angular momentum of the star $J_{\rm tot}/M^2$ during the evolution for three different grid resolutions: 120×60, 160×80 and 200×100 zones, respectively. The model used in the simulation is APR+DH 1.4.

different grid resolutions. When analysing the differences between the curves (see Section 5.1) we obtain the order of convergence of 1.95, which is near the expected second-order convergence. To estimate the absolute magnitude of the resulting angular momentum error we compare our perturbation to a rigidly rotating sphere with the same total angular momentum. Taking the typical total angular momentum during the simulation, and comparing it to that of a rigidly rotating sphere $J = 2/5MR^2\Omega = 2/5MRv_{\rm rot}$, where $\Omega = v_{\rm rot}/R$ is the rotation frequency, we obtain a maximal velocity which is only a fraction of the perturbation used in the simulations $v_{\rm rot}/v_{\rm pert} \sim 10^{-10}$. Thus, the total angular momentum introduced by our perturbation is very small. Moreover, the total angular momentum variations converge to zero, i.e. compared to the numerical errors the losses of angular momentum through the surface is a small effect not affecting our simulations.

5.4 QPO structure for high magnetic field strength

For strong magnetic fields we are interested in the structure of magnetoelastic QPOs, but not in the damping of crustal modes, as the latter are damped already at much lower field strengths (see Section 5.2). Therefore, we can reduce the grid resolution, i.e. the computational costs. In the strong field case we thus use a uniform radial grid with 100 zones and an angular grid with 80 zones in the interval $[0, \pi]$.

For very strong magnetic fields, $B \gtrsim 5 \times 10^{15}$ G, the maxima of the Fourier transform align towards the polar axis. With increasing magnetic field the influence of the shear inside the crust becomes negligible, and the QPO pattern approaches that expected for the purely magnetic limit (see fig. 3 in Cerdá-Durán et al. 2009), in agreement with the semi-analytic model. Another effect caused by the anisotropy of the shear modulus is a more widespread spatial structure of the QPOs compared to the case without crust. This can be inferred from the last two columns of Fig. 10, where QPOs are still quite extended inside the crust ($B = 8 \times 10^{15}$ G), and in the model without crust.

Between the two extremes, the QPOs are confined in the core ($B \lesssim 10^{15}$ G). For strong magnetic fields ($B \gtrsim 10^{15}$ G) there is a transition from the QPO structure observed in Section 5.3 to the purely magnetic case (see Fig. 10 from columns 3 to 6). Between 10^{15} and 2×10^{15} G the QPOs begin to have significant amplitudes in large parts of the crust.

This transition becomes clearer in Fig. 13, where we plot the Fourier amplitude for individual field lines averaged over the length of the line and labelled by their crossing point with the equatorial plane. The solid lines represent the continuum as obtained by the semi-analytic model, where we assume reflection at the crust–core interface in the upper row and reflection at the surface of the star in the lower row. The obtained frequencies are very similar in both cases, because the travel time of the waves is dominated by the time spent in the core. We note a change of the structure of the QPOs with the different boundary conditions. We have already noted in Fig. 10 that in the case of weak magnetic fields the QPOs move from being near the pole towards the equator, for increasing

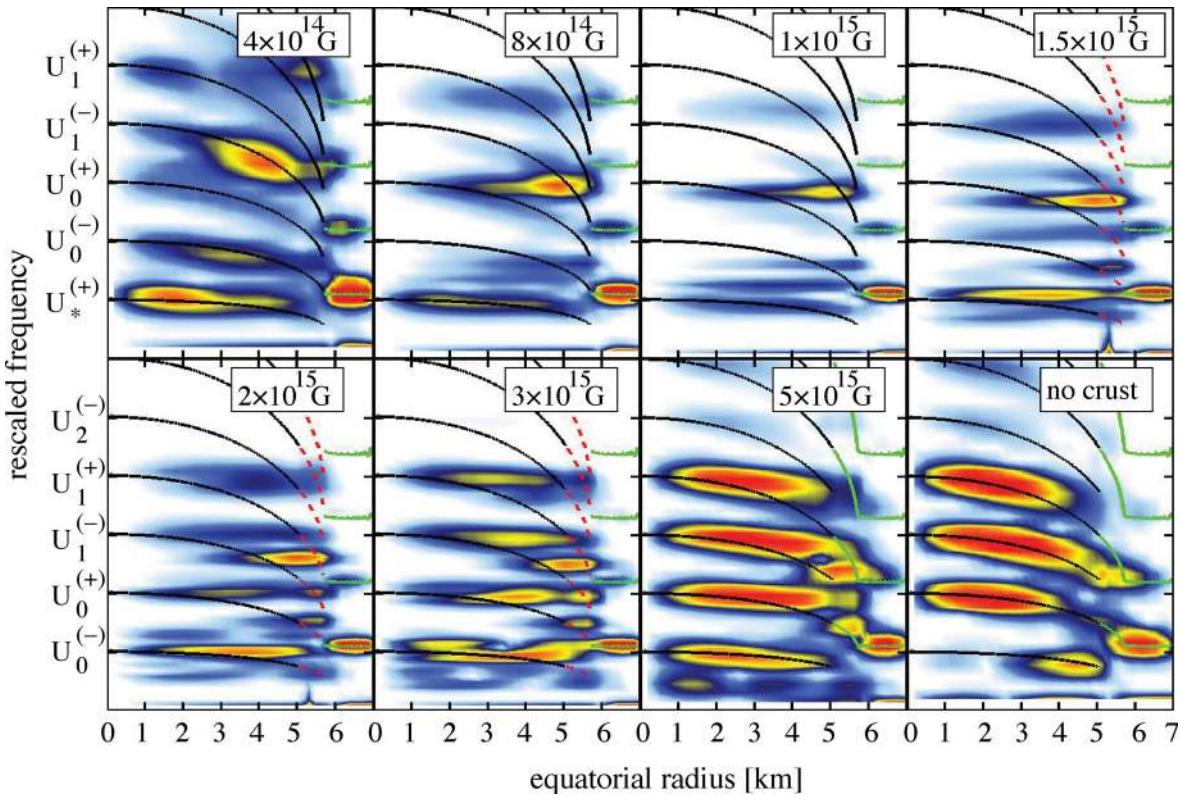

Figure 13. The averaged Fourier amplitude along different field lines labelled by the radius where they cross the equatorial plane for different magnetic field strengths. In the last panel we show the expected behaviour for a model without crust. The y-axis represents the frequency rescaled to the fundamental QPO frequency predicted by the semi-analytical model (see Table 5). The colour scale ranges from white-blue (minimum) to orange-red (maximum). Black and green lines represent the continuum when taking the crust into account. Dashed, red lines indicate regions where the semi-analytic model is not supposed to work. We do not know where the waves get reflected and thus cannot identify whether to consider the lines as open or closed.

magnetic field strength below 10^{15} G. The same can be observed in the first two panels of Fig. 13 for $U_0^{(-)}$, $U_1^{(-)}$ and $U_1^{(+)}$. Between 10^{15} and 2×10^{15} G a transition occurs from reflection at the crust–core interface (for weaker magnetic fields) and reflection at the surface of the star (for stronger fields). Therefore, we do not expect any of the two approximations to agree with the semi-analytic model. Neither can we assume that the oscillations get reflected only at the crust–core boundary nor only at the stellar surface. When increasing the magnetic field beyond 2×10^{15} G the maximum amplitude of the QPO aligns again towards the polar axis, and the numerically obtained pattern approaches the expected structure, which is similar to the case without the crust. The main differences are the presence of the fundamental $U_*^{(+)}$ at finite frequency and a broader maximum because of the anisotropic shear contribution. The QPOs are moving from the pole towards the equator according to the frequency predicted by the semi-analytic model for reflection at the crust–core interface, but when the effects of the magnetic field become comparable to those of the shear modulus in the crust, the QPOs reach the end of the continuum and *jump* from the symmetric (antisymmetric) branch to the antisymmetric (symmetric) branch of the next part of the continuum.

What happens to $U_*^{(+)}$, which has no possibility to jump to? For strong magnetic fields, $B \gtrsim 2 \times 10^{15}$ G $U_*^{(+)}$ has different features. First, there is no node along the field lines, due to the change of the boundary conditions, which require a maximum at the surface. Secondly, as can be seen in the last few columns of the upper row of Fig. 10, there are nodes perpendicular to the field lines at a given frequency, and we even find two different contributions to the $U_*^{(+)}$ at slightly different frequencies. Between 2×10^{15} and 5×10^{15} G there is one node perpendicular to the field lines, while for $B \geq 6 \times 10^{15}$ G the QPO has predominantly two nodes in that direction. Note that both features are always present for $B \gtrsim 2 \times 10^{15}$ G. This splitting can also be seen in the leftmost three panels of the lower row in Fig. 13. The corresponding features are located at frequencies below the fundamental, $U_0^{(-)}$. The same panels also show, that with increasing magnetic field strength, the relative Fourier amplitudes and the frequencies of those features decrease with respect to the fundamental frequency.

The picture of the transition from one asymptotic behaviour (reflection at the crust–core interface) to the other (reflection at the surface) gets supported by the frequencies obtained for the different QPOs shown in Table 5. There we compare the frequencies corresponding to the maxima of the Fourier amplitude with those of the fundamental oscillation obtained with the semi-analytic model. Thus, we use the version with reflection at the crust–core interface up to 10^{15} G, while we set the boundary at the surface of the star for stronger fields. For magnetic fields up to $B \lesssim 8 \times 10^{14}$ G, $U_*^{(+)}$ has a similar frequency as the fundamental obtained with the semi-analytic model. The frequencies of the other QPOs approximately behave as $1\,(U_*^{(+)}) : 3\,(U_0^{(+)}) : 5\,(U_1^{(+)})$ and $2\,(U_0^{(-)}) : 4\,(U_1^{(-)}) : 6\,(U_2^{(-)})$. For stronger magnetic fields $B \gtrsim 3 \times 10^{15}$ G the frequencies ratios approach $1\,(U_0^{(-)}) : 3\,(U_1^{(-)}) : 5\,(U_2^{(-)})$ and $2\,(U_0^{(+)}) : 4\,(U_1^{(+)})$. The two asymptotic integer relations between successive overtones and their order are what is expected from the semi-analytic model in the two regimes. In the intermediate regime $8 \times 10^{14} \lesssim B \lesssim 3 \times 10^{15}$ G the frequencies change smoothly from one relation to the other.

Deviations from exact integer ratios may have different reasons. First, the time of numerical integration is limited. Therefore, the spectral resolution of the Fourier analysis is limited, too. Secondly, for the lowest magnetic field shown here, $B \approx 2 \times 10^{14}$ G, not all upper QPOs have reached their position near the polar axis, i.e. their frequencies still lie in the continuum, resulting in lower frequencies. Thirdly, in particular in the transition regime it is sometimes difficult to identify where the maximum of a QPO is located. The interesting QPO may be excited only very weakly by our initial data, and/or some other QPO may be excited more strongly at a similar frequency. This occurs more frequently for higher overtones, because there the different continua overlap (see Fig. 8 or Fig. 13).

5.5 Crustal modes in the gaps of the Alfvén continuum?

van Hoven & Levin (2011) and Colaiuda & Kokkotas (2011) have pointed out the possibility of crustal modes, which may have frequencies outside of the continuum of the core. These modes would be only very weakly coupled to core oscillations, because no Alfvén wave of any field line could match the necessary frequency. In the models we have studied here, we find gaps in the continuum only between the lowest overtones of Alfvén oscillations (see Fig. 8), e.g. for model APR+DH 1.4 already the continua of $U_1^{(-)}$ and $U_1^{(+)}$ overlap and there are only gaps between $U_1^{(-)}$ and $U_0^{(+)}$, $U_0^{(+)}$ and $U_0^{(-)}$ and below $U_0^{(-)}$. For the other models shown in the Table 2 the number of gaps is limited to a maximum of about three for models with the crust EoS NV and to two for models with the DH EoS. Note

Table 5. The relation of the frequencies of the lowest QPOs for the model APR+DH 1.4, obtained by analysing the local maxima of the Fourier amplitudes, to the fundamental frequency U_0, obtained by the semi-analytic method. Note that the fundamental of the semi-analytic model changes symmetry at a magnetic field of about 10^{15} G, such that $U_0 \simeq U_*^{(+)}$ for $B \leq 10^{15}$ G and $U_0 \simeq U_0^{(-)}$ for $B > 10^{15}$ G. The last column shows the uncertainty in the separation of two successive frequencies in the Fourier spectrum. It gives an estimate of the error caused by choosing the position of the local maxima, but it does not include other numerical errors.

Polar magnetic field (G)	Frequency of fundamental U_0 with semi-analytic model (Hz)	$U_*^{(+)}/U_0$	$U_0^{(-)}/U_0$	$U_0^{(+)}/U_0$	$U_1^{(-)}/U_0$	$U_1^{(+)}/U_0$	$U_2^{(-)}/U_0$	$\delta U_n^{(\pm)}/U_0$
2×10^{14}	1.0	1.0	1.9	2.9	3.6	5.0	5.7	±0.24
4×10^{14}	2.0	1.0	1.8	2.8	3.5	4.9	5.5	±0.20
6×10^{14}	3.0	1.0	1.8	2.8	3.1	4.7	5.0	±0.10
8×10^{14}	4.0	1.0	1.8	2.5	3.5	4.3	5.1	±0.20
10^{15}	5.0	0.9	1.3	2.4	3.3	4.2	5.3	±0.10
1.5×10^{15}	7.4	0.8	1.1	2.2	3.2	4.1	5.1	±0.10
2×10^{15}	9.8	0.7	1.0	2.0	3.0	4.0	5.1	±0.10
3×10^{15}	14.7	0.5	0.9	2.0	3.0	4.0	5.1	±0.10
5×10^{15}	24.4	0.5	1.0	2.0	3.0	4.0	5.1	±0.10
8×10^{15}	39.1	0.3	0.9	2.0	3.0	4.1	5.1	±0.10

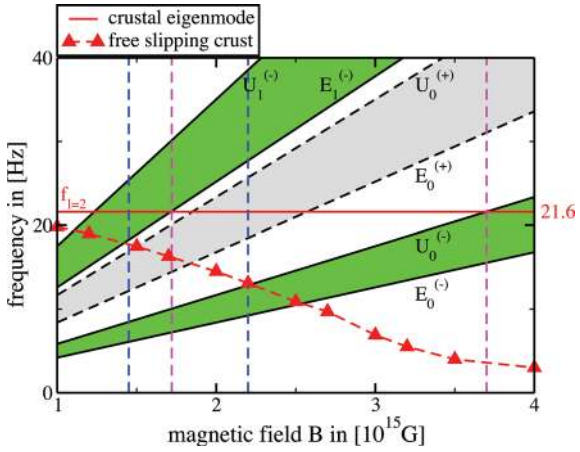

Figure 14. Frequency continua of model L+DH 1.4 at magnetic fields between $B = 10^{15}$ and 4×10^{15} G. Black, solid lines indicate the edges of the continua of the open field lines as indicated by the names $E_n^{(\pm)}$ and $U_n^{(\pm)}$. The horizontal red line gives the frequency of the $l = 2$ crustal shear mode and the dashed red lines give the frequency obtained by simulations with a free slipping crust (see text). The green shaded areas show continua having the same symmetry with respect to the equator as the $l = 2$ shear mode. The grey area shows the continuum with opposite symmetry. Magenta (blue) dashed lines show the range of magnetic field strengths where the frequency of the $n = 0, l = 2$ crustal mode lies in the gap between allowed Alfvén continua for purely shear modes (for free slipping crust with magnetic field).

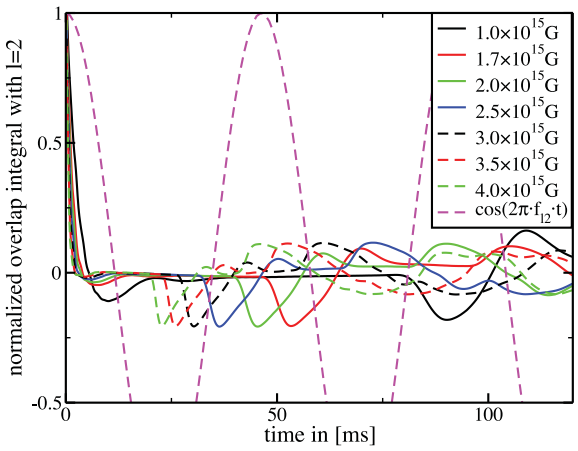

Figure 15. Evolution of the overlap integral of the $n = 0$, $l = 2$ mode of the crust at different magnetic field strengths: $B = \{1.0, 2.0, 2.5, 3.0, 3.5, 4.0\} \times 10^{15}$ G. The dashed magenta line shows the expected oscillation of the purely shear $l = 2$ mode of the crust. All other lines show strong damping of the excited $l = 2$ mode at early times ($t < 20$ ms). Contributions to the overlap integral at later times $t > 20$ ms originate from magnetoelastic oscillations.

that we only consider the continua of the open field lines indicated by the black lines in Fig. 8, because they are decoupled from the continua related to the closed field lines (green lines). To have the fundamental $n = 0, l = 2$ oscillation of the crust in one of the gaps, very strong magnetic fields $B > 10^{15}$ G are required.

As an example we choose the EoS L+DH 1.4, because the corresponding model has broader gaps than the APR+DH EoS. Furthermore, models with lower mass have shorter Alfvén crossing times, and therefore weaker magnetic fields are necessary to have the shear mode in the gap between the lowest overtones of the continua (see Table 7). The spectral structure of this model is displayed in Fig. 14, where we show the edges of the continua of the open field lines as a function of the magnetic field strength. The shaded areas between two edges represent the corresponding continuum, where crustal modes can be absorbed resonantly. The red line indicates the frequency 21.6 Hz of the purely shear, $n = 0, l = 2$ mode of the crust. Using model L+DH 1.4, we performed simulations with initial data with the crustal $n = 0, l = 2$ mode, allowing only for antisymmetry with respect to the equatorial plane. The oscillations of the continuum associated with symmetric QPOs, as for example $U_0^{(+)}$, are thus not allowed and cannot be excited. These forbidden oscillations are indicated by the grey shaded region in Fig. 14. We also confirmed that without imposing equatorial symmetry only Alfvén QPOs having the same symmetry as the corresponding crustal mode can be excited with significant amplitude during the evolution. Therefore, the antisymmetric $n = 0, l = 2$ shear mode of the crust lies in the gap between $U_0^{(-)}$ and $E_1^{(-)}$ for magnetic fields between 1.74 and 3.7×10^{15} G (Fig. 14). Following previous works by van Hoven & Levin (2011) or Colaiuda & Kokkotas (2011) the crustal mode in the gap should not be damped significantly, because there is no oscillation at the resonant frequency available in the continuum. However, we still find very strong damping of this crustal mode in our simulations, as indicated by the overlap integral of the $n = 0$, $l = 2$ shear mode in Fig. 15. Clearly the mode is damped after a few milliseconds for all considered magnetic field strengths. Later contributions originate from coupled magnetoelastic pulses travelling through the whole star. Therefore, the time when they contribute to the overlap integrals depends inversely on the magnetic field strength, a behaviour which is completely different from that of discrete oscillations for purely crustal shear modes. These observations indicate that we do not have a weakly coupled system of two subsystems (the crust and the core) but we are dealing with coupled, global magnetoelastic oscillations. To compare with what one would expect for an undamped purely crustal mode, we plotted the magenta, dashed line in Fig. 15.

We checked the influence of the magnetic field on the frequency of the purely shear mode by performing a series of simulations, where we apply an artificial boundary condition at the crust–core interface, i.e. we use the same condition $\xi_r^{\varphi} = 0$ that would apply in the absence of the magnetic field (see also Sotani et al. 2007). This allows the crust to slip freely on top of the core, and the oscillations inside the crust cannot be damped into the core. The frequency of the corresponding $l = 2$ crustal mode is influenced as displayed in Fig. 14. This is expected, because global, poloidal magnetic fields of the order of $B \sim 10^{15}$ G and stronger begin to have measurable effects (Duncan 1998; Messios, Papadopoulos & Stergioulas 2001; Sotani, Kokkotas & Stergioulas 2007; Sotani, Colaiuda & Kokkotas 2008a; Shaisultanov & Eichler 2009). Intuitively, one would expect the shear mode frequencies to increase with the magnetic field strength, because the magnetic tension could be interpreted as effectively augmenting the shear modulus (Messios et al. 2001; Sotani et al. 2007). In contrast to Sotani et al. (2007) we find a decrease of the $l = 2$ mode frequency with increasing dipolar magnetic field strength (see Fig. 14). In their work Sotani et al. (2007) neglected couplings between l and $l \pm 2$ modes due to the magnetic field, which led to discrete modes. However, by analysing the evolution of the corresponding overlap integrals we observe strong excitation of the $l = 4$ mode by the $l = 2$ mode in our simulations. This strong coupling may explain the opposite change of frequency than expected from the study by Sotani et al. (2007). For a different magnetic field configuration also Messios et al. (2001) and Sotani

et al. (2007) find that the frequency of the fundamental $l = 2$ crustal mode decreases with increasing magnetic field strength.

If the frequency of the $l = 2$ crustal mode changes according to our simulations with the free slipping crust, the magnetic field strengths for which the mode lies in the continuum gap is limited to 1.4×10^{15}–2.2×10^{15} G. In this regime we have performed four simulations at 1.5×10^{15}, 1.7×10^{15}, 2.0×10^{15} and 2.2×10^{15} G (triangles in Fig. 14). In all of them we find the strong damping of the crustal mode.

A second problem of matching of crustal frequencies into the gaps of the Alfvén continuum emerges at the field strengths ($\gtrsim 10^{15}$ G) at which we find the crustal frequencies in the continuum gaps, as there is no clear way of how to compute the Alfvén frequencies. In this transition regime, reflection neither occurs predominantly at the crust–core interface nor at the surface, therefore, we do not claim that the continuum shown in Fig. 14 is perfectly valid at all magnetic field strengths (compare the panels for 1.5×10^{15} G to those of 3×10^{15} G in Fig. 13). However, by performing simulations for 10 different magnetic field strengths between 10^{15} and 4×10^{15} G for the current model L+DH 1.4, we can ensure that the $l = 2$ crustal frequency lies in the gap between the Alfvén continua at least for one of the models. In none of the above simulations we find a different behaviour than the one reported, i.e. we do not observe any of the crustal shear modes. For crust models with lower shear modulus, we expect the transition to occur at lower magnetic field strength. The magnetic field required to fit a crustal shear mode into the gap between successive continua decreases with decreasing shear modulus. However, a smaller shear modulus also lowers the relative importance of the shear terms compared to the magnetic field.

In the example shown above, we may have just missed to match the frequency of the crustal mode to a gap of the continuum, as the frequency may have been changed due to the presence of the strong magnetic field, and because the continuum is probably not reliably predicted by the semi-analytic model. To this end we performed a large number (>50) of simulations at different magnetic field strengths $>10^{15}$ G and different equilibrium models but we never found any crustal shear mode at such strong magnetic fields.

Generalizing the dipolar magnetic field configuration, which is our main model simplification in the current context, would probably increase the complexity of the continuum, making it even harder to find gaps. However, there might arise new effects due to an entanglement of the magnetic field (see van Hoven & Levin 2011).

Crustal modes in the gaps of the Alfvén continua of the core have been reported by Colaiuda & Kokkotas (2011), but our results suggest that these QPOs are rather oscillations of the continuum. It is possible that the mode recycling technique (using the amplitude of the FFT at the frequency of the crustal shear modes) employed by Colaiuda & Kokkotas (2011) may give an excitation of the continuum at this frequency. van Hoven & Levin (2012) also observe gap modes. In their approach several one-dimensional eigenmodes of the magnetic field in the core are coupled to two-dimensional eigenmodes in the crust. However, they do not prove that their assumption that the crustal dynamics can be described with an eigenvalue problem is valid also in the presence of a magnetic field. Thus, we expect that the ansatz of van Hoven & Levin (2012) is valid only approximately for weak magnetic fields ($B < 10^{15}$ G). Such an eigenmode approach cannot describe the complicated coupling behaviour, including e.g. travelling wave packets, which would require the inclusion of a much larger number of coupled oscillators than those considered by van Hoven & Levin (2012).

5.6 Threshold for the outbreak of the QPOs through the crust

In Section 5.4 we noticed that for weak magnetic fields, $B \lesssim 10^{15}$ G, the QPOs are largely confined to the fluid core, and that there exists a threshold magnetic field strength beyond which QPOs can be observed with significant amplitudes at the surface of the star. To quantify when magnetoelastic QPOs have a significant amplitude in the crust of the neutron star, we studied their maximum amplitude at the surface. In Fig. 16 we plot the amplitude of the Fourier transform at the surface for different magnetic field strengths as a function of the polar angle θ and the frequency. The colour scaling is rescaled in each panel to enhance the main contributions at each magnetic field strength. We consider APR+DH 1.4 as our reference model. First we note that for very strong fields ($>5 \times 10^{15}$ G) the frequencies approach those predicted by the semi-analytic model, because the influence of the crust should decrease for increasing magnetic field strength. There is some low-frequency oscillation which corresponds to $U_*^{(+)}$ (compare with Fig. 13), and there are some additional, strong Fourier modes near to $\pi/2$ resulting from the edge modes, which are stronger than in the case without crust.

However, when decreasing the strength of the magnetic field from 5×10^{15} to 2×10^{15} G, the Fourier amplitude of the QPOs at the surface decreases, e.g. the maximum decreases from 1.0 to 0.37 in units normalized to the maximum amplitude at $B = 5 \times 10^{15}$ G. As we have already seen in Fig. 10, this is expected, because for decreasing field strength the crust will shield the QPOs. We further see that the additional structure in the Fourier amplitude at about the fundamental frequency of $U_0^{(-)}$ and the strong feature just below the frequency of $U_1^{(-)}$ close to the equator are increasing in amplitude relative to the upper QPOs. We note here that in the transition

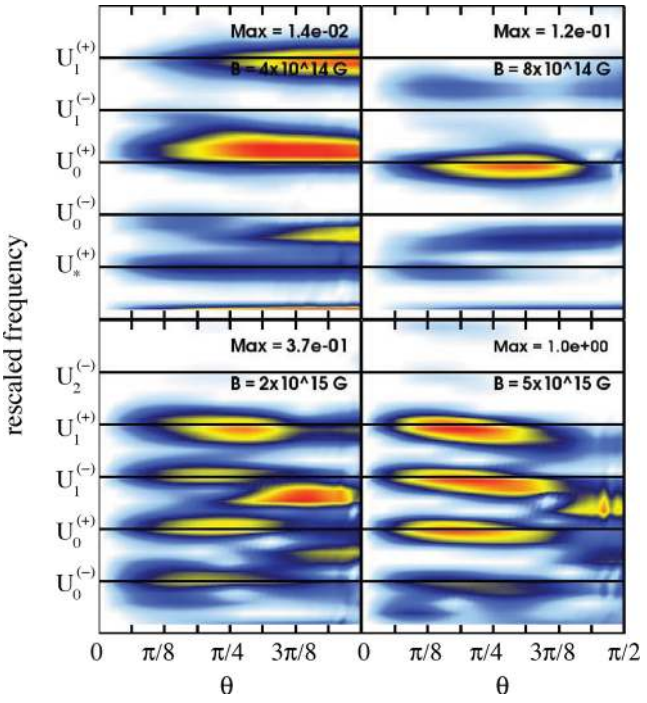

Figure 16. Normalized amplitude of the Fourier transform at the surface of the star (between pole and equator) as a function of the frequency for the stellar model APR+DH with $1.4\,M_\odot$. The horizontal lines indicate the frequency for the upper QPOs predicted by the semi-analytic model. The colour scale ranges from white-blue (minimum) to orange-red (maximum).

Table 6. The maximal magnitude of the Fourier transform at the surface of the star for a dipole magnetic field strength of 10^{15} G. Simulations for different EoS, and with and without crust are considered and compared.

Model	$\frac{\text{FFT}(10^{15}\text{ G})}{\text{FFT (no crust)}}$	Model	$\frac{\text{FFT}(10^{15}\text{ G})}{\text{FFT (no crust)}}$
APR+DH 1.4	0.07	APR+NV 1.4	0.06
APR+DH 1.8	0.11	APR+NV 1.8	0.005
APR+DH 2.2	0.33	APR+NV 2.2	0.04
L+DH 1.4	0.16	L+NV 1.4	0.016
L+DH 1.8	0.36	L+NV 1.8	0.03
L+DH 2.2	0.15	L+NV 2.2	0.009

region of magnetic field strengths the correspondence between the frequencies of the semi-analytic model and the simulated QPOs should be taken with caution and we do not expect a simple QPO structure as in the two limiting cases.

When decreasing the magnetic field strength towards 8×10^{14} G a dominant feature originates from $U_0^{(+)}$. In a sequence of similar plots for different magnetic fields not shown here, one can follow the slight change in frequency until reaching approximately the value predicted by the semi-analytic model for reflection at the crust–core interface. Comparing with Fig. 10 the corresponding spatial structure of the mode has still some amplitude inside the crust, i.e. our interpretation in terms of the $U_0^{(+)}$ QPO makes sense. The general trend is that the magnetoelastic upper QPOs exhibit a decreasing amplitude near the surface for decreasing magnetic field strength.

For the weakest magnetic field (4×10^{14} G), the upper QPOs have no strong amplitudes, because they are confined to the fluid core. The dominant contribution at the surface results from the edge modes in this case (see Fig. 7). The QPO with the largest amplitude inside the crust is the edge QPO $E_2^{(+)}$ (see Fig. 16) with a frequency slightly above $U_0^{(+)}$ (see also the right-hand panel of Fig. 8). Other contributions to the Fourier signal at the surface stem from the two edge QPOs $E_1^{(+)}$ and $E_3^{(+)}$ at frequencies just below $U_0^{(-)}$ and close to $U_1^{(+)}$, respectively. However, the edge QPOs are damped much faster than turning point QPOs, and the amplitude in the Fourier analysis for the same initial data is about two orders of magnitude smaller than for a reference model without crust. Therefore we doubt that edge QPOs are the explanation for the observed frequencies in SGR for magnetic fields $B \lesssim 5 \times 10^{14}$ G. In Table 6 we give the maximum of the Fourier amplitude at the surface for a simulation with crust at 10^{15} G with respect to the corresponding simulation without crust. The closer this value is to 1.0 the stronger is the amplitude of the QPO at the surface. For very low values the crust shields the QPOs efficiently, i.e. they are confined to the core of the neutron star. For the DH crustal EoS there is already a considerable amount of oscillations penetrating the crust and reaching the surface. We therefore argue that magnetoelastic oscillations break through the crust around 10^{15} G. However, for the NV EoS the amplitudes for models with crust never reach 10 per cent of the values for models without crust, as the crust is more extended in this case, and QPOs can break through the crust only for even stronger magnetic fields. Nevertheless, the threshold of $B \sim 10^{15}$ G should be a good approximation for all models. Interestingly, this result is comparable with estimates of the magnetic field strengths for SGRs showing giant flares.

6 SUMMARY AND DISCUSSION

We have presented results from two-dimensional, general relativistic magnetohydrodynamical simulations of neutron stars with an extended solid crust, in continuation of our initial results communicated as a letter (Gabler et al. 2011). Performing a comprehensive set of simulations for several neutron star models and EoS, we have been able to confirm our previous findings regarding the QPO structure for three different regimes of the magnetic field strength. Our main results can be summarized as follows.

(i) For weak magnetic fields, $B \lesssim 5 \times 10^{13}$ G, purely shear oscillations of the crust dominate the evolution in the latter. For intermediate magnetic field strengths, $5 \times 10^{13} \lesssim B \lesssim 10^{15}$ G, the $n = 0$ crustal modes are damped very efficiently into the core of the neutron star on time-scales of a fraction ($\sim$0.04) of the Alfvén crossing time of the star. For example, a model with $B = 10^{14}$ G has a damping time-scale of $\tau < 100$ ms. This effectively rules out purely shear oscillations of the crust as a possible explanation for the observed QPOs in SGRs for the poloidal magnetic field configurations studied here, since the observed QPOs survive for tens of seconds at estimated magnetic field strengths $B \gtrsim 6 \times 10^{14}$ G. We find a damping time-scale dependence on the magnetic field which scales as $\sim B^{-1}$, dominated by the ability of the Alfvén continuum to absorb the energy of crustal modes.

(ii) In comparison to the $n = 0$ modes, the $n > 0$ modes of the crust have damping time-scales of order hundreds of milliseconds at around 5×10^{14} G. The spatial structure of the $n > 1$ modes becomes significantly distorted in the presence of such a strong magnetic field. However, predictions for even stronger magnetic fields, $B > 5 \times 10^{14}$ G, are currently not possible, because the grid resolution needed to couple the $n > 0$ shear modes to Alfvén oscillations in the core is too high to perform simulations in reasonable time. We thus cannot safely exclude the $n > 0$ crustal shear modes as possible explanation for the high frequency QPOs observed in SGR 1806−20 at 625 and 1840 Hz, if the magnetic field is a purely dipolar one.

(iii) For magnetic fields, $B \gtrsim 5 \times 10^{14}$ G, we find no sign of the existence of discrete crustal shear modes. This is in contrast to the results of the model of van Hoven & Levin (2011), who proposed that weakly damped global QPOs, resembling purely crustal shear modes in the zero magnetic field limit, may survive if the corresponding shear mode frequency lies in-between adjacent continua. In the most promising of our models we find gaps between the first four continua, but even when choosing the equilibrium model so that the fundamental crustal mode frequency falls in one of the existing gaps, we found that the mode was damped very efficiently by the coupling to the Alfvén continuum in the core. Furthermore, at dipolar magnetic field strengths $B \gtrsim 10^{15}$ G, necessary to fit the frequencies of crustal shear modes into a gap, we expect that the magnetic field begins to have significant influence on the shear oscillations of the crust (Messios et al. 2001; Sotani et al. 2008a; Shaisultanov & Eichler 2009). Our findings strongly support the interpretation that for high magnetic field strengths magnetar oscillations are a strongly coupled magnetoelastic system, where a division into purely crustal modes and Alfvén oscillations is no longer valid.

(iv) In the intermediate magnetic field regime ($5 \times 10^{13} \lesssim B \lesssim 10^{15}$ G) the QPOs are largely confined to the core of the neutron star. We find three families of QPOs: upper, edge and lower QPOs. Their spatial structure coincides very well with the expectations from our semi-analytic model, if we assume that the oscillations are reflected

at the crust–core boundary. Together with the strong damping of the crustal shear modes, the reflection of Alfvén QPOs at the crust–core interface leads to very small oscillation amplitudes in the crust. Moreover, when changing the magnetic field strength, the position of the maximum of the corresponding upper QPO within the star changes significantly due to the interaction with the crust.

(v) We have also determined the dipolar magnetic field strength at which the magnetoelastic QPOs break through the crust and reach the surface with significant amplitudes. This happens around $B \sim 10^{15}$ G for the DH crust EoS and at slightly stronger magnetic fields for the NV crust EoS. This difference can be understood easily, because the NV EoS leads to thicker crusts and larger shear moduli, in particular near the crust–core interface.

(vi) Between $10^{15} \lesssim B \lesssim 5 \times 10^{15}$ G the QPOs are still transforming from being confined to the core to being able to reach the surface and the QPOs have spatial structures different from those at much lower or much higher magnetic field strengths. Colaiuda & Kokkotas (2011) report global, discrete Alfvén modes in gaps between continua, at magnetic fields around 4×10^{15} G. In our model, this is still in the above transition regime, and the reported oscillations are not discrete Alfvén modes, but rather an effect of the transition between the two limiting regimes.

(vii) For dipolar magnetic field strengths $B \gtrsim 5 \times 10^{15}$ G the magnetoelastic oscillations have an almost Alfvén-like character in the whole star and the role of the shear modulus in the crust is diminished, recovering the results of Sotani et al. (2008b) and Cerdá-Durán et al. (2009).

The model we have presented allows for a tentative interpretation of the observed QPOs in terms of the predominantly Alfvén QPOs which reach the surface. The main family of QPOs we expect to play a role in the observed QPOs are the upper (turning point) QPOs. As first pointed out by Sotani et al. (2008a), the interpretation of the frequencies 30, 92 and 150 Hz in SGR 1806−20 in terms of the $U_0^{(-)}$, $U_1^{(-)}$ and $U_2^{(-)}$ QPOs is very tempting. Here we note that the 18 Hz oscillation may be interpreted as the first edge QPO $E_0^{(-)}$, which for model APR+DH has a frequency of about 0.57 $f_{U_0^{(-)}} \approx 17$ Hz (this could also correspond to the frequency at 16.9 Hz found by Hambaryan et al. 2011). Similarly, the 36.4 Hz oscillation could be interpreted as the $E_1^{(-)}$ QPO. However, one should be cautious with these latter identifications, since edge QPOs are not as long-lived as turning point QPOs.

If we require that the fundamental upper QPO matches the observed 30 Hz QPO in SGR 1806−20 or the 28 Hz QPO in SGR 1900+14, we obtain mean dipolar magnetic field strengths at the surface in the possible range $3.8 \times 10^{15} \lesssim B \lesssim 1.1 \times 10^{16}$ G (for the particular choices of EoS and masses) as reported in Table 7. This is a rather narrow range and it is at only somewhat larger magnetic field strengths than simple estimates for magnetic fields in known magnetars.

We conclude by highlighting that our model provides two different constraints on the magnetic field strength. The first constraint is that the dipolar magnetic field strength must be larger than $B \sim 10^{15}$ G for QPOs to break out of the crust, which is a lower limit on the magnetic field. This constraint is independent of a particular identification of observed QPOs and only depends on the assumed magnetic field structure of a pure dipole. The second constraint comes from the matching of the lowest frequency observed QPO, that appears at near-integer multiples, with the fundamental $U_0^{(-)}$ QPO. This constrains the mean dipolar magnetic field strength at the surface of the neutron star to be in the range of $3.8 \times 10^{15} \lesssim B \lesssim 1.1 \times 10^{16}$ G for the sample of EoSs and various masses that we assumed here.

Table 7. Mean surface magnetic field strength required to match the frequency of the fundamental Alfvén QPO to 30 Hz observed in SGR 1806−20 and 28 Hz of SGR 1900+14.

Model	$B_{30\,\mathrm{Hz}}$ (10^{15} G)	$B_{28\,\mathrm{Hz}}$ (10^{15} G)
APR+DH 1.4	5.0	4.6
APR+DH 1.8	7.1	6.6
APR+DH 2.2	11.0	10.3
L+DH 1.4	4.1	3.8
L+DH 1.8	5.5	5.1
L+DH 2.2	6.4	6.7
APR+NV 1.4	5.1	4.8
APR+NV 1.8	7.4	6.9
APR+NV 2.2	11.3	10.6
L+NV 1.4	4.6	4.4
L+NV 1.8	6.2	5.8
L+NV 2.2	8.1	7.6

The above constraints, favouring somewhat stronger magnetic fields than estimated for known magnetars, hint at a possible deviation of the actual magnetic field structure from a global dipole. This is not surprising, as it is known that a purely dipolar or purely toroidal field is not a stable magnetic field configuration in compact stars (see Braithwaite & Nordlund 2006; Ciolfi et al. 2011; Kiuchi, Yoshida & Shibata 2011; Lasky et al. 2011, and references therein). We may thus have an observational indication that the structure of the magnetic field in magnetars is in fact more complicated than a pure dipole. Other physical effects that may cause the magnetic field required to match the magnetoelastic QPOs to the range of observed frequencies to be weaker, are superfluidity of the neutrons and superconductivity of the protons in the core.

We are planning to investigate the effects produced by changing the magnetic field configuration and those caused by superfluidity and superconductivity of the neutrons and protons in the core, which are expected to influence the Alfvén speeds and the overall dynamics (Passamonti & Andersson 2012). For the former, we need to investigate different dipolar configurations, mixed poloidal–toroidal configurations, relax the assumption of axisymmetry and include the coupling to polar oscillations. Moreover, the coupling to an exterior magnetosphere, where the X-ray emission is modulated, also has to be included in a complete model.

ACKNOWLEDGMENTS

We thank A. Colaiuda for fruitful discussions about the interpretation of the simulations and F. Lamb for drawing our attention to the possibility of different realizations of dipolar magnetic fields. This work was supported by the Collaborative Research Center on Gravitational Wave Astronomy of the Deutsche Forschungsgemeinschaft (DFG SFB/Transregio 7), the Spanish Ministerio de Educación y Ciencia (AYA 2010-21097-C03-01) and the Generalitat Valenciana (PROMETEO-2009-103), a DAAD exchange grant for MG for an extended visit at the Aristotle University of Thessaloniki and by CompStar, a Research Networking Programme of the European Science Foundation. The computations were performed at the Servicio de Informática de la Universidad de Valencia.

REFERENCES

Akmal A., Pandharipande V. R., Ravenhall D. G., 1998, Phys. Rev. C, 58, 1804
Blaes O., Blandford R., Goldreich P., Madau P., 1989, ApJ, 343, 839
Bocquet M., Bonazzola S., Gourgoulhon E., Novak J., 1995, A&A, 301, 757
Bonazzola S., Villain L., Bejger M., 2007, Classical Quantum Gravity, 24, 221
Braithwaite J., Nordlund Å., 2006, A&A, 450, 1077
Carter B., Quintana H., 1972, Proc. R. Soc. Lond. Ser. A, 331, 57
Carter B., Samuelsson L., 2006, Classical Quantum Gravity, 23, 5367
Cerdá-Durán P., 2010, Classical Quantum Gravity, 27, 205012
Cerdá-Durán P., Font J. A., Antón L., Müller E., 2008, A&A, 492, 937
Cerdá-Durán P., Stergioulas N., Font J. A., 2009, MNRAS, 397, 1607
Ciolfi R., Lander S. K., Manca G. M., Rezzolla L., 2011, ApJ, 736, L6
Colaiuda A., Kokkotas K. D., 2011, MNRAS, 414, 3014
Colaiuda A., Beyer H., Kokkotas K. D., 2009, MNRAS, 396, 1441
Demorest P. B., Pennucci T., Ransom S. M., Roberts M. S. E., Hessels J. W. T., 2010, Nat, 467, 1081
Dimmelmeier H., Font J. A., Müller E., 2002a, A&A, 388, 917
Dimmelmeier H., Font J. A., Müller E., 2002b, A&A, 393, 523
Dimmelmeier H., Novak J., Font J. A., Ibáñez J. M., Müller E., 2005, Phys. Rev. D, 71, 064023
Douchin F., Haensel P., 2001, A&A, 380, 151
Duncan R. C., 1998, ApJ, 498, L45
Duncan R. C., Thompson C., 1992, ApJ, 392, L9
El-Mezeini A. M., Ibrahim A. I., 2010, ApJ, 721, L121
Gabler M., Sperhake U., Andersson N., 2009, Phys. Rev. D, 80, 064012
Gabler M., Cerdá-Durán P., Font J., Müller E., Stergioulas N., 2010, J. Phys. Conf. Ser., 283, 012013
Gabler M., Cerdá Durán P., Font J. A., Müller E., Stergioulas N., 2011, MNRAS, 410, L37
Glampedakis K., Andersson N., 2006, MNRAS, 371, 1311
Hambaryan V., Neuhäuser R., Kokkotas K. D., 2011, A&A, 528, A45
Isenberg J. A., 2008, Int. J. Modern Phys. D, 17, 265
Israel G. L. et al., 2005, ApJ, 628, L53
Karlovini M., Samuelsson L., 2003, Classical Quantum Gravity, 20, 3613
Karlovini M., Samuelsson L., 2004, Classical Quantum Gravity, 21, 4531
Karlovini M., Samuelsson L., 2007, Classical Quantum Gravity, 24, 3171
Karlovini M., Samuelsson L., Zarroug M., 2004, Classical Quantum Gravity, 21, 1559
Kiuchi K., Yoshida S., Shibata M., 2011, A&A, 532, A30
Lander S. K., Jones D. I., 2011, MNRAS, 412, 1730
Lander S. K., Jones D. I., Passamonti A., 2010, MNRAS, 405, 318
Lasky P. D., Zink B., Kokkotas K. D., Glampedakis K., 2011, ApJ, 735, L20
Lee U., 2007, MNRAS, 374, 1015
Lee U., 2008, MNRAS, 385, 2069
Levin Y., 2006, MNRAS, 368, L35
Levin Y., 2007, MNRAS, 377, 159
Levin Y., van Hoven M., 2011, MNRAS, 418, 659
Messios N., Papadopoulos D. B., Stergioulas N., 2001, MNRAS, 328, 1161
Negele J. W., Vautherin D., 1973, Nuclear Phys. A, 207, 298
Pandharipande V. R., Smith R. A., 1975, Phys. Lett. B, 59, 15
Papadopoulos D., Esposito F. P., 1982, ApJ, 257, 10
Passamonti A., Andersson N., 2012, MNRAS, 419, 638
Piro A. L., 2005, ApJ, 634, L153
Rea N. et al., 2010, Sci, 330, 944
Samuelsson L., Andersson N., 2007, MNRAS, 374, 256
Schumaker B. L., Thorne K. S., 1983, MNRAS, 203, 457
Shaisultanov R., Eichler D., 2009, ApJ, 702, L23
Sotani H., Kokkotas K. D., Stergioulas N., 2007, MNRAS, 375, 261
Sotani H., Colaiuda A., Kokkotas K. D., 2008a, MNRAS, 385, 2161
Sotani H., Kokkotas K. D., Stergioulas N., 2008b, MNRAS, 385, L5
Steiner A. W., Watts A. L., 2009, Phys. Rev. Lett., 103, 181101
Strohmayer T. E., Watts A. L., 2005, ApJ, 632, L111
Strohmayer T., van Horn H. M., Ogata S., Iyetomi H., Ichimaru S., 1991, ApJ, 375, 679
Thompson C., Duncan R. C., 2001, ApJ, 561, 980
van Hoven M., Levin Y., 2011, MNRAS, 410, 1036
van Hoven M., Levin Y., 2012, MNRAS, doi:10.1111/j.1365-2966.2011.20177.x
Watts A. L., Strohmayer T. E., 2007, Advances Space Res., 40, 1446
Wilson J. R., Mathews G. J., Marronetti P., 1996, Phys. Rev. D, 54, 1317

APPENDIX A: ALTERNATIVE NUMERICAL METHOD

In this appendix we derive a wave equation to describe the coupled crust–core oscillations of magnetars. To this end we expand all dynamical variables $f(\boldsymbol{r},t)$ into a static unperturbed part $\hat{f}(\boldsymbol{r})$, denoted by a caret, and a time-dependent perturbation $\delta f(\boldsymbol{r},t)$:

$$f(\boldsymbol{r},t) = \hat{f}(\boldsymbol{r}) + \delta f(\boldsymbol{r},t). \tag{A1}$$

For clarity we will omit the arguments $\boldsymbol{r}$ and t from now on.

In the subsequent subsections we derive the equation for the displacement, describe the numerical implementation and compare the performance of this alternative method with the standard approach using Riemann solvers on both sides of the crust–core interface.

A1 Linear wave equation

To derive the linearized wave equation governing the evolution of the displacement in the crust of a magnetized neutron star, we project the conservation equation of energy–momentum:

$$h^{\mu}_{\beta} T^{\beta\nu}_{\ ;\nu} = 0, \tag{A2}$$

$$\begin{aligned}(\rho h + b^2) u^{\mu}_{\ ;\nu} u^{\nu} = &-h^{\mu\nu}\left(P + \tfrac{1}{2}b^2\right)_{;\nu} \\ &+ h^{\mu}_{\beta}(b^{\beta}b^{\nu} - 2\mu_{\rm S}\Sigma^{\beta\nu})_{;\nu},\end{aligned} \tag{A3}$$

with $h^{\mu\nu} = g^{\mu\nu} + u^{\mu}u^{\nu}$ and apply the following simplifications: (i) we linearize in the perturbations δf and (ii) neglect all metric perturbations (Cowling approximation, $\delta g = 0$). Then equation (A2) reads

$$\begin{aligned}&(\hat{\rho}\hat{h} + \hat{b}^2)\delta u^{\mu}_{\ ;\nu}\hat{u}^{\nu} \\ &= -\left(\delta\rho\hat{h} + \hat{\rho}\delta h + 2\hat{b}_{\beta}\delta b^{\beta}\right)\hat{u}^{\mu}_{\ ;\nu}\hat{u}^{\nu} - (\hat{\rho}\hat{h} + \hat{b}^2)\hat{u}^{\mu}_{\ ;\nu}\delta u^{\nu} \\ &\quad + \left(\hat{u}^{\mu}\delta u_{\beta} + \delta u^{\mu}\hat{u}_{\beta}\right)\left[\hat{b}^{\beta}\hat{b}^{\nu} - \hat{g}^{\beta\nu}\left(\hat{P} + \tfrac{1}{2}\hat{b}^2\right)\right]_{;\nu} \\ &\quad + \hat{h}^{\mu}_{\beta}\left[\hat{b}^{\beta}\delta b^{\nu} + \delta b^{\beta}\hat{b}^{\nu} - \hat{g}^{\beta\nu}(\delta P + \hat{b}_{\beta}\delta b^{\beta})\right]_{;\nu} \\ &\quad - 2\hat{h}^{\mu}_{\beta}\left[\delta\mu_{\rm S}\hat{\Sigma}^{\beta\nu} + \hat{\mu}_{\rm S}\delta\Sigma^{\beta\nu}\right]_{;\nu}.\end{aligned} \tag{A4}$$

Next we restrict ourselves to (iii) axisymmetry ($f_{,\varphi} = 0$), and (iv) axial perturbations ($\delta u^t = \delta u^r = \delta u^{\theta} = 0$, $\delta b^r = \delta b^{\theta} = 0$ and $\delta\mu_{\rm S} = \delta h = \delta\rho = \delta P = 0$). Furthermore, we consider (v) the spherical symmetric, non-rotating background described by the line element $\mathrm{d}s^2 = -\hat{\alpha}^2\mathrm{d}t + \hat{\Phi}^4(\mathrm{d}r^2 + r^2\mathrm{d}\theta^2 + r^2\sin(\theta)^2\mathrm{d}\varphi^2)$, and (vi) purely poloidal background fields ($\hat{b}^{\varphi} = 0$). Applying all these simplifications one arrives at the following equation for δu^{φ}:

$$\begin{aligned}(\hat{\rho}\hat{h} + \hat{b}^2)\hat{u}^t\delta u^{\varphi}_{\ ,t} = &\ \hat{b}^r\delta b^{\varphi}_{\ ,r} + \hat{b}^{\theta}\delta b^{\varphi}_{\ ,\theta} - 2\hat{\mu}_{\rm S}\delta\Sigma^{\varphi\nu(s)}_{\ \ ;\nu} \\ &+ \delta b^{\varphi}\left[\left(\frac{2\hat{\Phi}_{,r}}{\hat{\Phi}} + \frac{2}{r} + \frac{\hat{\alpha}_{,r}}{\hat{\alpha}}\right)\hat{b}^r + 2\cot(\theta)\hat{b}^{\theta}\right].\end{aligned} \tag{A5}$$

Because of the dependence of $\Sigma^{\mu\nu}$ on the displacement ξ^{φ}, we express all other quantities in terms of the latter. Recalling the definition of the corresponding velocity $\xi^{\varphi}_{\ ,t} = \delta u^{\varphi}/\hat{u}^t$, see equation (24), the perturbed magnetic field δb^{φ} remains the only missing ingredient.

To find an expression relating δb^φ to ξ^φ, we contract the Faraday equation:

$$(u^\mu b^\nu - u^\nu b^\mu)_{;\mu} = 0, \tag{A6}$$

with u_ν and obtain

$$u_\nu b^\nu_{;\mu} u^\mu = u^\nu_{;\mu} u_\nu b^\mu - b^\mu_{;\mu}, \tag{A7}$$

where we have used $u_\nu u^\nu = -1$ and $u_\nu b^\nu = 0$. From $u_\nu b^\nu_{;\mu} u^\mu = 0$ (see Papadopoulos & Esposito 1982) it follows that

$$b^\mu_{;\mu} = u^\nu_{;\mu} u_\nu b^\mu. \tag{A8}$$

When linearizing equation (A6) and using (A8) Faraday's equation becomes

$$\begin{aligned}\hat{u}^\mu \delta b^\nu_{;\mu} = &-\hat{b}^\nu_{;\mu}\delta u^\nu + \hat{h}^{\nu\beta}(\delta u_{\beta;\lambda}\hat{b}^\lambda + \hat{u}_{\beta;\lambda}\delta b^\lambda)\\ &+ \hat{u}^\nu \delta u^\beta \hat{b}^\lambda \hat{u}_{\beta;\lambda} - \delta u^\mu_{;\mu}\hat{b}^\nu - \hat{u}^\mu_{;\mu}\delta b^\nu\\ &+ \hat{u}^\nu \hat{b}^\beta(\delta u_{\beta;\lambda}\hat{u}^\lambda + \hat{u}_{\beta;\lambda}\delta u^\lambda)\\ &+ \hat{u}_{\beta;\lambda}\hat{u}^\lambda(\hat{b}^\beta \delta u^\nu + \delta b^\beta \hat{u}^\nu).\end{aligned} \tag{A9}$$

Taking the φ-component of this equation, we arrive at a relation between δb^φ and the spatial derivatives of the displacement ξ^φ which reads

$$\begin{aligned}\hat{u}^t \delta b^\varphi_{,t} &= \tfrac{\hat{\alpha}_{,r}}{\hat{\alpha}}\hat{b}^r \delta u^\varphi + \hat{b}^r \delta u^\varphi_{,r} + \hat{b}^\theta \delta u^\varphi_{,\theta}\\ &= \hat{b}^r \hat{u}^t \left(\frac{\hat{\alpha}_{,r}}{\hat{\alpha}}\xi^\varphi_{,t} + \xi^\varphi_{,t,r}\right) + \hat{b}^\theta \hat{u}^t \xi^\varphi_{,t,\theta}\\ &\quad + \hat{b}^r \hat{u}^t{}_{,r}\xi^\varphi_{,t}\end{aligned} \tag{A10}$$

or

$$\delta b^\varphi_{,t} = \left(\hat{b}^r \xi^\varphi_{,r} + \hat{b}^\theta \xi^\varphi_{,\theta}\right)_{,t}, \tag{A11}$$

where we have used that $\hat{u}^t = \hat{\alpha}^{-1}$. Plugging this relation into equation (A5) we obtain

$$\begin{aligned}\hat{A}_0 \xi^\varphi_{,tt} = &\hat{A}_1 \xi^\varphi_{,r} + \hat{A}_2 \xi^\varphi_{,\theta} + \left(\hat{b}^\theta \hat{b}^\theta + \frac{\hat{\mu}_S}{r^2\hat{\Phi}^4}\right)\xi^\varphi_{,\theta\theta}\\ &+(2\hat{b}^r\hat{b}^\theta)\xi^\varphi_{,\theta r} + \left(\hat{b}^r\hat{b}^r + \frac{\hat{\mu}_S}{\hat{\Phi}^4}\right)\xi^\varphi_{,rr},\end{aligned} \tag{A12}$$

with

$$\hat{A}_0 = (\hat{\rho}\hat{h} + \hat{b}^2)(\hat{u}^t)^2, \tag{A13}$$

$$\begin{aligned}\hat{A}_1 = &\hat{A}_3\hat{b}^r + \hat{b}^r\hat{b}^r{}_{,r} + \hat{b}^\theta\hat{b}^r{}_{,\theta} + \left(\frac{\hat{\mu}_S}{\hat{\Phi}^4}\right)_{,r}\\ &+\left(\frac{\hat{\alpha}_{,r}}{\hat{\alpha}} + 10\frac{\hat{\Phi}_{,r}}{\hat{\Phi}} + \frac{4}{r}\right)\frac{\hat{\mu}_S}{\hat{\Phi}^4},\end{aligned} \tag{A14}$$

$$\begin{aligned}\hat{A}_2 = &\hat{A}_3\hat{b}^\theta + \hat{b}^r\hat{b}^\theta{}_{,r} + \hat{b}^\theta\hat{b}^\theta{}_{,\theta} + \left(\frac{\hat{\mu}_S}{r^2\hat{\Phi}^4}\right)_{,\theta}\\ &+3\cot(\theta)\frac{\hat{\mu}_S}{r^2\hat{\Phi}^4}\end{aligned} \tag{A15}$$

and

$$\hat{A}_3 = \left(4\frac{\hat{\Phi}_{,r}}{\hat{\Phi}} + \frac{2}{r} + \frac{\hat{\alpha}_{,r}}{\hat{\alpha}}\right)\hat{b}^r + 2\cot(\theta)\hat{b}^\theta. \tag{A16}$$

The solution of the coefficient determinant of the second-order derivatives of equation (A12),

$$0 = a_{ij}|x^i||x^j|\frac{\partial^2\xi}{\partial x^i \partial x^j} = c_{ij}\frac{\partial^2\xi}{\partial x^i \partial x^j}, \tag{A17}$$

$$c_{ij} = \begin{pmatrix}\hat{\alpha}^2\hat{A}^0 & 0 & 0\\ 0 & \hat{\Phi}^4\hat{b}^r\hat{b}^r + \frac{\hat{\mu}_S}{r^2} & \hat{\Phi}^4 r\hat{b}^r\hat{b}^\theta\\ 0 & \hat{\Phi}^4 r\hat{b}^\theta\hat{b}^r & \hat{\Phi}^4 r^2\hat{b}^\theta\hat{b}^\theta + \mu_S\end{pmatrix}, \tag{A18}$$

leads to the following eigenvalues:

$$\lambda_1 = 1, \tag{A19}$$

$$\lambda_2 = \frac{\hat{\mu}_S + \hat{b}^2}{\hat{\alpha}^2\hat{A}_0}, \tag{A20}$$

$$\lambda_3 = \frac{\hat{\mu}_S}{\hat{\alpha}^2\hat{A}_0}, \tag{A21}$$

where the eigenvector corresponding to λ_2 (λ_3) is oriented along (perpendicular to) the magnetic field lines, i.e. they correspond to the linearized version of equation (31). All eigenvalues are real, and hence equation (A12) is hyperbolic.

A2 Numerical implementation of the linearized wave equation in the crust

As when using Riemann solvers on both sides of the crust–core interface, the equations and the numerical scheme in the fluid core of the neutron star remain unmodified. In order to evolve equation (A12) numerically in the crust we split it into two equations for ξ^φ and $\xi^\varphi_{,t}$, and then perform an explicit Runge–Kutta integration. Since we are now evolving two systems with different variables in the core and in the crust, we have to impose interface conditions.

The evolutions computed with this method rapidly become unstable when increasing the magnetic field strength. It was therefore necessary to add some artificial dissipation. We used a fourth-order Kreiss–Oliger term $\epsilon_D \mathcal{D}_4 f$, where $\mathcal{D}_4 f$ is the fourth-order numerical derivative of any function f. The minimal coefficient found to give stable evolutions is $\epsilon_D = 10^{-2}$. We checked the code to ensure that this additional term does not influence the results of the simulations significantly.

A3 Comparison of the two methods

To compare the results of the crustal mode damping (see Section 5.2) obtained with the two numerical methods presented in Sections 2 and 4 and in Appendix A we plot the evolution of the velocity at some point in the crust near the pole (Fig. A1). Without magnetic field, the linear method is less dissipative, which is probably related to the set-up of the interface conditions at the crust–core interface in this particular case. While we use the general conditions described in Section 4 for the Riemann solver approach, it is possible to use a simplified expression for the linear method. Because there is no magnetic field the expression of continuous traction at the crust–core interface leads to $\xi^\varphi_{,r} = 0$ as at the surface. This provides a source of dissipation for the Riemann solver method, but none for the linear approach. In the presence of magnetic fields the picture changes, and the evolution computed with the Riemann solver has less dissipation of crustal modes than the linear method (see Fig. A1). When using different coefficients in the Kreiss–Oliger term, the curves for the linear method are indistinguishable. We can therefore rule out that the artificial dissipation dominates the numerical damping observed for the linear approach.

Because of its superior behaviour in the more generic case we generally used the Riemann solver method to obtain the numerical results. We checked that the linear approach agrees on the extracted

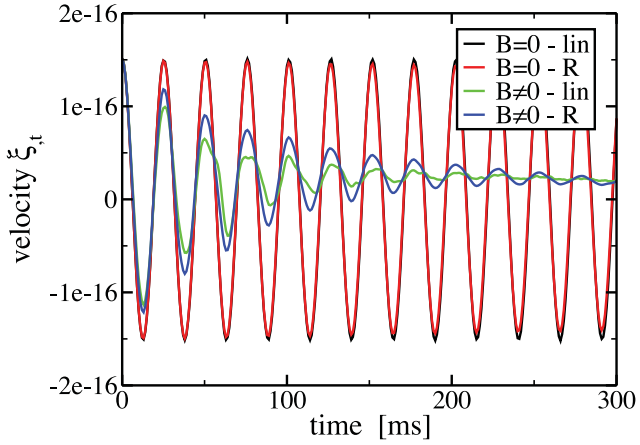

Figure A1. Evolution of the velocity $\xi_{,t}$ at some point in the crust near the pole for $B = 5 \times 10^{13}$ G and without a magnetic field. The two different numerical methods are denoted by *lin* for the linear method and *R* for the Riemann solver approach. The linear method is less dissipative for zero magnetic field, while the opposite holds when the magnetic field is turned on.

frequencies with the Riemann solver for all regimes of the magnetic field strength considered by us.

APPENDIX B: EIGENMODES IN THE CRUST

Without magnetic field equation (A12) simplifies to

$$\hat{A}_0 \xi^{\varphi}_{,tt} = \hat{A}_1 \xi^{\varphi}_{,r} + \hat{A}_2 \xi^{\varphi}_{,\theta} + \frac{\hat{\mu}_S}{r^2 \hat{\Phi}^4} \xi^{\varphi}_{,\theta\theta} + \frac{\hat{\mu}_S}{\hat{\Phi}^4} \xi^{\varphi}_{,rr} = \nabla_\nu \left(\mu_S g^{\nu\nu} \xi^{\varphi}_{,\nu} \right), \tag{B1}$$

with

$$\hat{A}_0 = \hat{\rho} \hat{h} (\hat{u}^t)^2, \tag{B2}$$

$$\hat{A}_1 = \left(\frac{\hat{\mu}_S}{\hat{\Phi}^4} \right)_{,r} + \hat{C} \frac{\hat{\mu}_S}{\hat{\Phi}^4}, \tag{B3}$$

$$\hat{A}_2 = \left(\frac{\hat{\mu}_S}{r^2 \hat{\Phi}^4} \right)_{,\theta} + 3 \cot(\theta) \frac{\hat{\mu}_S}{r^2 \hat{\Phi}^4} \tag{B4}$$

and

$$\hat{C} = \frac{\hat{\alpha}_{,r}}{\hat{\alpha}} + 10 \frac{\hat{\Phi}_{,r}}{\hat{\Phi}} + \frac{4}{r}. \tag{B5}$$

Assuming a harmonic time dependence $\xi^{\varphi}(\boldsymbol{r}, t) = \xi^{\varphi}(\boldsymbol{r}) e^{i\omega t}$ and a separation of variables $\xi^{\varphi}(r, \theta) = R(r)\Theta(\theta)$ leads to

$$-\omega^2 \hat{A}_0 = \left[\left(\frac{\hat{\mu}_S}{r^2 \hat{\Phi}^4} \Theta'(\theta) \right)_{,\theta} + 3 \cot(\theta) \frac{\hat{\mu}_S}{r^2 \hat{\Phi}^4} \Theta'(\theta) \right] \frac{1}{\Theta(\theta)} + \left[\left(\frac{\hat{\mu}_S}{\hat{\Phi}^4} R'(r) \right)_{,r} + \hat{C} \frac{\hat{\mu}_S}{\hat{\Phi}^4} R'(r) \right] \frac{1}{R(r)}, \tag{B6}$$

where a prime denotes the derivative with respect to the corresponding variable r or θ. The angular and radial part have to fulfil this equation independently, such that

$$0 = \Theta''(\theta) + 3 \cot\theta \Theta'(\theta) + \lambda_\theta^2 \Theta(\theta), \tag{B7}$$

$$0 = \frac{\hat{\mu}_S}{\hat{\Phi}^4} R''(r) + \left[\left(\frac{\hat{\mu}_S}{\hat{\Phi}^4} \right)_{,r} + \hat{C} \frac{\hat{\mu}_S}{\hat{\Phi}^4} \right] R'(r) + \lambda_r^2 R(r), \tag{B8}$$

where $\lambda_r^2 = \left(\omega^2 \hat{A}_0 + \lambda_\theta^2 \right)$. Both equations are of singular Sturm–Liouville type, and therefore their solutions R_{λ_r} and Θ_{λ_θ} form a complete, orthonormal set $\Xi_i(r, \theta) = R_{\lambda_r} \Theta_{\lambda_\theta}$. The solution of the angular part consists of the angular part of the vector spherical harmonics $\Psi_n(\theta)$, which is related to the Legendre polynomials $P_n(\theta)$ by

$$\Psi_n(\theta) \sim \frac{\partial P_n(\theta)}{\partial \theta}. \tag{B9}$$

The equation to obtain $R(r)$ is solved numerically with a shooting method. Because the eigenfunctions $\Xi_i(r, \theta)$ form a complete set, it is possible to expand any displacement in terms of the former:

$$\xi^{\varphi}(r, \theta, t) = \sum_i A_i(t)\ \Xi_i(r, \theta), \tag{B10}$$

where the eigenmode coefficients $A_i(t)$ are given by the inner product:

$$A_i(t) = \langle \xi^{\varphi}(r, \theta, t), \Xi_i(r, \theta) \rangle = \int_{r_{cc}}^{r_s} \xi^{\varphi}(r, \theta, t)\ \Xi_i(r, \theta) w_\theta w_r \mathrm{d}r\, \mathrm{d}\theta. \tag{B11}$$

The corresponding weighting functions w_r and w_θ are, according to the Sturm–Liouville theory,

$$w_\theta = \sin(\theta)^3, \tag{B12}$$

$$w_r = \frac{\alpha(r)^{-1} \Phi(r)^{10}\ r^4 \rho(r) h(r)}{\alpha(r_{cc})^{-1} \Phi(r_{cc})^{10}\ r_{cc}^4 \rho(r_{cc}) h(r_{cc})}. \tag{B13}$$

We calculate the overlap integrals defined in equation (B11) with a fourth-order Simpsons rule algorithm.

This paper has been typeset from a TEX/LATEX file prepared by the author.